Hindawi
Shock and Vibration
Volume 2021, Article ID 9928168, 28 pages
https://doi.org/10.1155/2021/9928168

Research Article

Numerical Investigation of Relationship between Bursting Proneness and Mechanical Parameters of Coal

Hongwei Wang,[1,2] **Jiaqi Song**,[1] **Zeliang Wang**,[1] **Yue Zhang**,[1] **Shaozhen Zhang**,[1] **and Yaodong Jiang**[1,3]

[1]*School of Mechanics and Civil Engineering, China University of Mining and Technology, Beijing 100083, China*
[2]*State Key Laboratory for Geomechanics and Deep Underground Engineering, China University of Mining & Technology, Beijing 100083, China*
[3]*State Key Laboratory of Coal Resources and Safe Mining, China University of Mining & Technology, Beijing 100083, China*

Correspondence should be addressed to Hongwei Wang; whw@cumtb.edu.cn

Received 16 March 2021; Accepted 17 May 2021; Published 1 June 2021

Academic Editor: Haiyan Wang

Copyright © 2021 Hongwei Wang et al. This is an open access article distributed under the Creative Commons Attribution License, which permits unrestricted use, distribution, and reproduction in any medium, provided the original work is properly cited.

As one of the most catastrophic dynamic hazards in underground coal mines, coal bursts have been a major safety concern around the world for many years. Although the coal bursts can occur in all cases of hard to soft coal if the right stress environment is created, the occurrence of coal bursts is closely related to the intrinsic mechanical properties of coal, such as the bursting proneness. In this study, a total of 27 coal specimens are selected in the open literature studies to obtain a group of fundament data, such as the mechanical parameters, four bursting proneness indices, stress-strain curves, and their geological conditions where the specimens were taken. The relationship between bursting proneness indices and the cohesion of the coal specimens is established by numerically fitting the stress-strain curves and theoretically deduction. By taking into account the coal heterogeneity, eight probability distribution functions are employed to assignment nonuniform cohesion to the numerical model and to study the influence of heterogeneity on bursting proneness. The results reveal that the coal cohesion, which combines the common advantages of the four proneness indices, can be used as bursting proneness index. In the research of heterogeneity, the coal bursting proneness will decrease with the increasing of cohesion scatter degree. The larger the cohesion scatter degree increase is, the lower the bursting proneness will be. The failure of coal specimen is more and more severe with the decrease of cohesion scatter degree. In addition, this paper provides two methods for assigning heterogeneous parameters to the numerical model. The contours of shear strain rate and plastic state between homogeneous and heterogeneous coal specimens are compared to study the failure types of coal specimens and to reveal the mechanism of violent failure in coal bursts.

1. Introduction

As one of the most catastrophic dynamic hazards in an underground coal mine, coal bursts have been a major safety concern around the world for many years [1–8]. The sudden and violent failure of coal and rock masses accompanied by loud noise and ground vibration frequently occurs during the coal bursts. For example, on October 20, 2018, a severe coal burst accident occurred in the Longyun coal mine, Shandong Province, China, and resulted in heavy casualties and serious disruption to the mine operations [9]. In addition, in 2010 and 2011, two serious coal burst accidents occurred successively in Yima mining area in China caused casualties, equipment damage, and economic losses [10]. Between 1983 and 2017, 283 coal burst accidents were reported to the Mine Safety and Health Administration (MSHA) in the United States [10]. In 2014, two miners were killed and the mining machine was severely damaged in a coal burst accident in the Austar coal mine in New South Wales, Australia [11, 12].

There are a large number of factors associated with the occurrence of coal bursts. However, although the coal bursts

can occur in all cases of hard to soft coal if the right stress environment is created, the occurrence of coal bursts is closely related to the intrinsic mechanical properties of coal, such as the bursting proneness [13–16]. Generally, the bursting proneness is determined by a group of indices including uniaxial compressive strength (R_c), elastic strain energy (W_{ET}), bursting energy (K_E), and dynamic fracturing duration (D_t) [17–21]. Kidybiński used these four indices to study the ability of coal seam to store and release elastic strain energy and evaluate and classify the coal burst risk [18]. By tracing the progressive fracture process of rock material and studying the stress-strain curve in the uniaxial compressive tests, Lippmann reviewed the advantage and limitation of these four bursting proneness indices [19]. Haramy and McDonnell pointed out that coal had the capacity to store strain energy and highly recommended the use of the elastic strain energy index (W_{ET}) to evaluate the ability of coal to burst [20]. Singh conducted a series of tests to search a parameter which can be used to measure the burst proneness of coal and suggested that the burst energy index (K_E) be used as the main index in assessing the burst prone [21]. Lee et al. used elastic strain energy (W_{ET}) to evaluate high-potential rockburst in a tunnel with overburden depth greater than 400 m [22]. Su et al. employed these indices to evaluate the bursting proneness of coal seam in the Chengjiao coal mine in China and studied the correlation among these indices [23]. Wang et al. investigated the intrinsic properties of coal by these indices and studied the relationship between the intrinsic and external factors contributing to the occurrence of coal bursts [3].

As Kidybinski stated, the bursting proneness was the natural ability of coal to store and release elastic strain energy. Therefore, the bursting proneness of coal is an issue of distribution between energy storage and release. To gain in-depth understanding of the relationship between the bursting proneness and coal bursts, apart from these four indices, numerous studies have been carried out to obtain novel bursting proneness indices based on the investigation of energy storage and release, e.g., surplus energy [24–26], modified brittleness [27], and energy dissipation indices [24, 28], burst energy speed [29], and energy release speed [30]. Zhang et al. put forward an index of residual energy emission speed to evaluate the released energy per second [25]. Qi et al. pointed out that the brittleness index and moisture content of coal material can also be used to study the coal burst proneness [31]. Based on studying the relation between busting strain energy and wave velocity, Cai et al. introduced a bursting strain energy index to quantitatively map the coal burst risk contour in a coal mine in China and they developed a fuzzy comprehensive evaluation method by considering the results of microseismic monitoring [32]. Faradonbeh and Taheri intended to assess the coal burst risk by three novel indices including genetic algorithm-based emotional neural network (GA-ENN) and gene expression programming (GEP) [33]. By considering a current available database, Afraei et al. presented aggregative predictor variables combining the overburden thickness, tensile strength, and brittleness ratio of rock strata [34]. Gale pointed out that coal burst was related to the energy available and rib side resistance and comprehensively used indices of burst velocity, strain energy resistance, seismic energy, and gas energy to evaluate the coal burst risk [35]. Gong et al. proposed a residual elastic energy index to quantitatively study the relationship between stored elastic energy density, dissipated energy density, and total input energy density [26].

In fact, the bursting proneness of coal is closely related to the internal composition and microstructure of coal [6, 36–38]. Zhang et al. revealed that the burst proneness was related to the heterogeneous degree of rock material [36]. Similarly, Feng and Zhao pointed out that the intrinsic properties of coal with bursting proneness depended on the microscopic homogeneity of rock or coal [39]. Pan et al. revealed that the joint density is closely related to the ability of the rock mass to store high strain energy. The higher the joint density is, the weaker the ability to accumulate the elastic strain energy of rock mass is and the lower the rockburst proneness is [40]. Pan et al. revealed that the composition and structure inside the rock played an important role on the bursting proneness of rock and found that the strength and Young's modulus of rock masses would increase with the increase of the noncrystalline quartz content and decrease with the increase of the montmorillonite and kaolinite [5, 41]. Su et al. conducted a series of uniaxial compressive tests and found that crack propagation in coal specimen with high bursting proneness was extremely violent [42]. Wang et al. indicated that the coal sample with high bursting proneness contained large amounts of noncrystalline quartz [6]. Song et al. studied the strength, components, and microstructures of coal specimen by the methods of scanning electron microscopy (SEM) and electromagnetic radiation (EMR) and found that the failure characteristics of burst coal was regarded as brittle failure because of the heterogeneous composition and microstructure [43].

According to the review of literature studies about the bursting proneness indices and relationship between bursting proneness and microstructure of material, it can be seen that the current studies of bursting proneness are mainly focused on the proneness index definition and application. However, there is limited information available in the open literature about the relationship between the indices R_c, W_{ET}, K_E, and D_t. In fact, there is a common mechanical parameter among the four indices, which is of great significance to assessing the bursting proneness. In addition, although the effectiveness of material composition and microstructure on the bursting proneness has been investigated for many years, there is little information about the numerical method for simulating the distribution of heterogeneous parameters, failure types of heterogeneous coal specimens, and its influence on the mechanism of violent failure in coal bursts. In this study, a total of 27 coal specimens are selected in the open literature studies to obtain a group of fundament data, such as the mechanical parameters, four bursting proneness indices, stress-strain curves, and their geological conditions where the specimens were taken. The relationship between bursting proneness indices and the cohesion of the coal specimens is established

by numerically simulation and theoretically deduction. The reason that cohesion can be used as an index to assess the bursting proneness is analyzed based on the in-depth understanding on the common advantages of the four proneness indices. By taking into account the coal heterogeneity, the nonuniform distribution of cohesion in coal specimens is mapped by eight commonly used probability distribution functions to study the influence of heterogeneity on bursting proneness. In addition, the internal and external factors contributing to coal bursts are analyzed to reveal the mechanism of occurrence of coal bursts.

2. Overview of Coal Specimens with Bursting Proneness Selected from Open Literature Studies

2.1. Standard Indices and Classification of Bursting Proneness. Bursting proneness is an inherent property of coal. It is used to evaluate the risk of coal bumps by assessing the energy accumulation capability of coal. According to the current standard in China, bursting proneness is classified into three levels: high, low, and none [17]. The standard proneness indices include the elastic strain energy index (W_{ET}), the bursting energy index (K_E), the duration of dynamic fracture (D_t), and uniaxial compressive strength (R_c) [18, 21, 33].

As shown in Figure 1, these four indices are determined by conducting the uniaxial compressive tests. The uniaxial compressive strength (R_c) is the peak stress of stress and strain curve (Figure 1(a)). The elastic strain energy index (W_{ET}) (Figure 1(b)) is the ratio of the elastic energy accumulated, and the dissipated plastic energy before 80–90% of the peak strength of the coal is achieved. The bursting energy index (K_E) (Figure 1(c)) is defined as the ratio of the strain energy accumulated before peak strength and the strain energy released after peak strength. The larger the elastic strain energy index and bursting energy index are, the higher the bursting proneness of the coal will be. The duration of dynamic fracture (D_t) (Figure 1(d)) refers to the time span from peak strength to complete failure of coal specimen and is expressed in milliseconds. Since the index D_t represents the speed of accumulated energy release, the smaller the value of D_t is, the higher the bursting proneness of coal will be. Table 1 presents the classification of the bursting proneness of coal with the indices of R_c, W_{ET}, K_E, and D_t.

2.2. Coal Specimens with Bursting Proneness. A total of 27 coal specimens are taken from the open literature to establish a group of fundament data of the stress-strain curves and bursting proneness indices of specimens [23, 42, 44–49]. As the uniaxial compressive tests in these references are conducted under the same testing standard, the data from these tests are collected and sequenced in order of the values of uniaxial compressive strength (UCS), as listed in Table 2. In this study, the USC is actually the bursting proneness index R_c. The elastic strain energy index (W_{ET}), the bursting energy index (K_E), and the duration of dynamic fracture (D_t) of these coal specimens are also listed. The comprehensive results of bursting proneness are determined according to the current standard in Table 1. Among the 27 specimens, 17 specimens are of high bursting proneness, 6 are of low bursting proneness, and 4 coal specimens are of none bursting proneness. Table 2 also lists the geological conditions of the coal mines in which these specimens were taken. For example, the geological conditions of the Qianqiu coal mine in Yima mining area, Henan Province, China, are characterized with the occurrence of large synclines, reverse fault structures, and extreme thick roof strata [38, 44, 50].

The stress-strain curves of these 27 coal specimens in the uniaxial compressive tests were also obtained, as shown in Figure 2. These curves are grouped and shown into nine subfigures based on coal mines at which specimens were taken. It should be noted that the bursting proneness results obtained from the stress-stain curves merely represent the mechanical characteristics of these 27 specimens rather than the coal seam in these nine coal mines.

Although the stress-strain curves and bursting proneness are gained in the uniaxial compressive tests, it is impossible to obtain other important parameters of the specimens such as Young's modulus, cohesion, friction angle, and tensile strength through the same tests. In this study, the 27 stress-strain curves will be numerically fitted to obtain these parameters.

3. Correlation between Bursting Proneness and Mechanical Parameters of Coal

3.1. Numerical Model and Simulation Scheme. According to the ISRM-suggested methods for rock mechanics, a cylinder with diameter of 50 mm and height of 100 mm is built in ANSYS (Analysis Systems). This ANSYS model is then transferred into FLAC^{3D} (Fast Lagrangian Analysis of Continua in 3-Dimensions) code as the numerical model for simulation, as shown in Figure 3. In this numerical model, FLAC^{3D} mesh elements with size of 2.2 mm × 1.4 mm × 2.5 mm are presented.

The failure criterion is the strain-softening model which is based on the Mohr–Coulomb model with nonassociated shear and associated tension flow rules. In this model, the cohesion, friction, and tensile strength may soften after the onset of plastic yield by a user-defined piecewise linear function. Since Young's modulus, Poisson's ratio, cohesion, friction angle, and tensile strength of the 27 coal specimens were not given in the cited literature studies, the initial mechanical parameters are empirically determined according to the UCS, as listed in Table 3 [51]. Based on the stress-strain curve in Figure 2, the numerical curves will be fitted by adjusting the initial parameter until curves are well fitted with a set of appropriate parameters which are then taken as the parameters of the specimens.

A coordinate system is selected with the x- and y-axes located in the base of the cylinder and the z-axis pointing along the cylinder axis. On the basis of applying fixed displacement boundary conditions at the bottom of model, a constant velocity of 5×10^{-5} mm/step is applied in the z-direction at top of the cylinder to induce compression of the specimen, as shown in Figure 3.

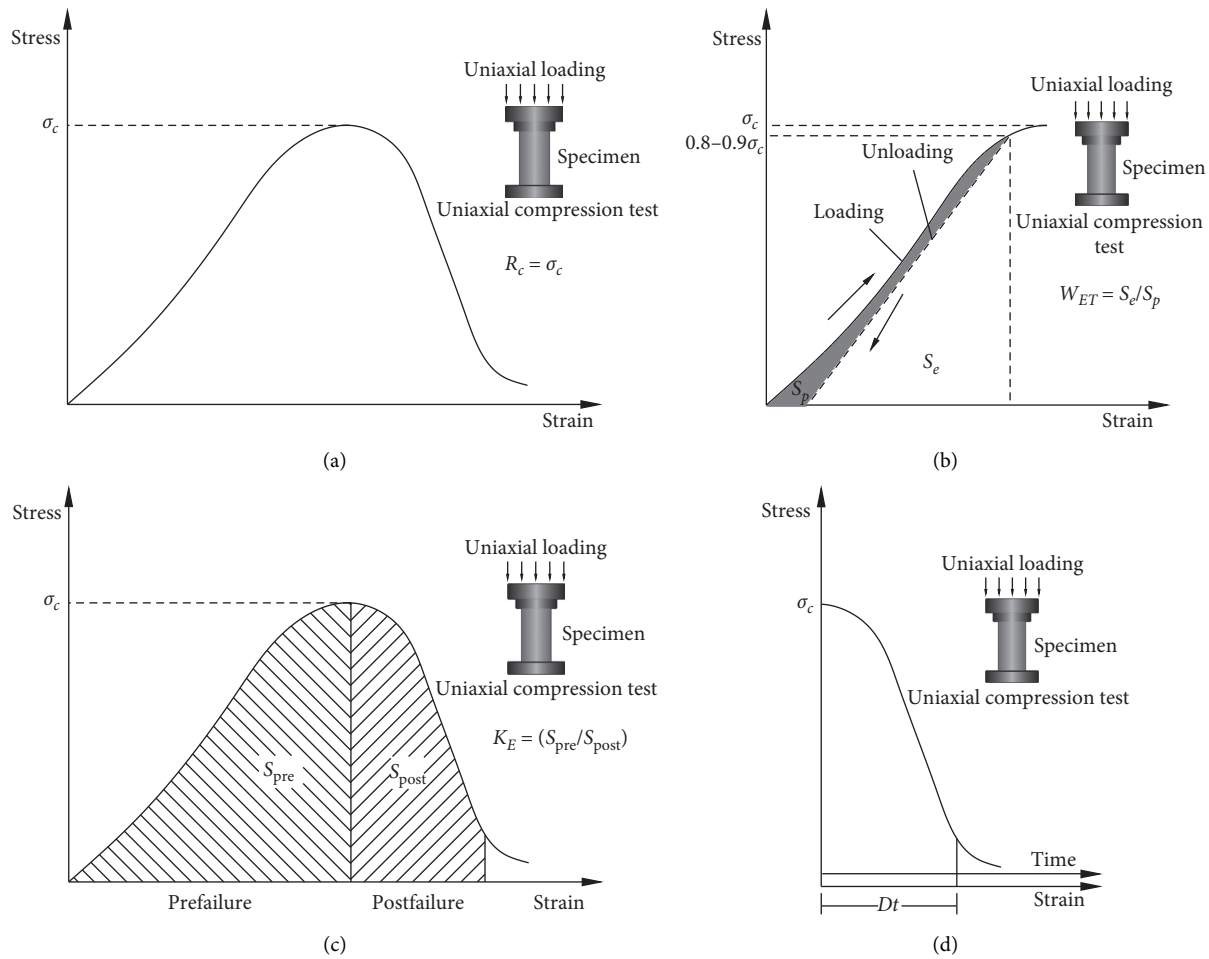

Figure 1: Four indices obtained from the uniaxial compressive test and employed to classify the bursting proneness of coal: (a) uniaxial compressive strength (R_c); (b) elastic strain energy index (W_{ET}); (c) bursting energy index (K_E); (d) duration of dynamic fracture (D_t).

Table 1: Classification of the bursting proneness of coal and indices according to current standard in China [17].

Indices	No bursting proneness	Low bursting proneness	High bursting proneness
Elastic energy index (W_{ET})	$W_{ET} < 2$	$2 \le W_{ET} < 5$	$W_{ET} \ge 5$
Bursting energy index (K_E)	$K_E < 1.5$	$1.5 \le K_E < 5$	$K_E \ge 5$
Dynamic rupture period (Dt) (ms)	$Dt > 500$	$50 < Dt \le 500$	$Dt \le 50$
Uniaxial compressive strength (R_c)	$R_c < 7$	$7 \le R_c < 14$	$R_c \ge 14$

In this study, the numerical simulation is performed according to the following procedure:

Step 1: numerical fitting of the stress-strain curves of the 27 coal specimens with uniform distribution of mechanical parameters.

Step 2: to obtain the mechanical parameters of the 27 coal specimens, e.g., Young's modulus, Poisson's ratio, cohesion, friction angle, tensile strength, and uniaxial compressive strength.

Step 3: study on heterogeneity by probability distribution.

Step 4: nonuniform parameter assignment to the numerical model.

Step 5: study of the influence of nonuniform distribution of mechanical parameters on UCS of coal specimen.

Step 6: study of coal bursting proneness and failure.

3.2. Numerical Fitting of Stress-Strain Curve and Relevant Parameters. Figure 4 presents the numerical fitted stress-strain curves of the 27 specimens. In order to ensure the accuracy of the fitting results, the fitting degree between the numerical fitting curve and the experimental curve is calculated. The fitting degree refers to the fitting degree of the regression line to the observed value. The statistical measure of the goodness of fit is the determinable coefficient (also

Table 2: Coal specimens and values of bursting proneness indices accompanied by geological conditions of the sites from which the specimens were taken.

Specimens	Bursting proneness					Coal mine	Location	Geological conditions	Reference
	R_c	W_{ET}	K_E	D_t	Results				
No. 1	27.26	9.36	12.02	12.11	High	Zhaogu	Henan, China	Large amounts of faults and subsidiary fold structures	Su et al. [42]
No. 2	25.13	8.12	7.49	23.75	High	Tangshan	Hebei, China	Existence of primary folds and large amounts of island longwall mining face	Pan et al. [44]
No. 3	24.58	7.52	7.79	31.56	High	Tangshan	Hebei, China	Existence of primary folds and large amounts of island longwall mining face	Pan et al. [44]
No. 4	22.70	7.70	9.82	45.78	High	Mentougou	Beijing, China	Existence of thrust faults and overturned rock strata. Fold structures such as syncline and anticline existed alternately	Okubo et al. [47]
No. 5	21.24	7.84	5.98	29.51	High	Tangshan	Hebei, China	Existence of primary folds and large amounts of island longwall mining face	Pan et al. [44]
No. 6	21.08	7.25	13.44	22.70	High	Mentougou	Beijing, China	Existence of thrust faults and overturned rock strata. Fold structures such as syncline and anticline existed alternately	Okubo et al. [47]
No. 7	20.68	7.51	6.91	56.27	High	Sanjiaohe	Shanxi, China	A series of developed folds and subsidiary faults existence	Li et al. [46]
No. 8	20.39	6.12	13.26	51.68	High	Pingdingshan	Henan, China	A series of faults and folds existence	Su et al. [48]
No. 9	20.33	7.02	4.93	29.87	High	Mentougou	Beijing, China	Existence of thrust faults and overturned rock strata. Fold structures such as syncline and anticline existed alternately	Okubo et al. [47]
No. 10	20.24	6.97	5.80	28.78	High	Pingdingshan	Henan, China	Large amounts of faults and subsidiary fold structures	Su et al. [48]
No. 11	19.53	7.53	5.19	49.79	High	Zhaogu	Henan, China	Large amounts of faults and subsidiary fold structures	Su et al. [42]
No. 12	18.65	6.91	4.26	45.41	High	Zhangcun	Shanxi, China	Coal seams existed in a monocline fold structure	Su et al. [49]
No. 13	16.71	6.34	3.35	38.88	High	Qianqiu	Henan, China	Large synclines, reverse fault structures, and extreme thick roof strata	Pan et al. [44]
No. 14	16.65	6.29	5.12	42.32	High	Chengjiao	Henan, China	Wide and gentle slope fold structures accompanied by a number of faults	Su et al. [23]
No. 15	16.09	5.85	3.59	25.32	High	Qianqiu	Henan, China	Large synclines, reverse fault structures, and extreme thick roof strata	Pan et al. [44]
No. 16	15.82	5.45	2.87	50.88	High	Qianqiu	Henan, China	Large synclines, reverse fault structures, and extreme thick roof strata	Pan et al. [44]
No. 17	14.88	5.83	4.62	58.19	High	Zhangcun	Shanxi, China	Coal seams existed in a monocline fold structure	Su et al. [49]
No. 18	12.40	4.60	2.40	167.23	Low	Pingdingshan	Henan, China	A series of faults and folds existence	Su et al. [48]
No. 19	11.46	4.78	3.59	26.45	Low	Chengjiao	Henan, China	Wide and gentle slope fold structures accompanied by a number of faults	Su et al. [23]
No. 20	11.03	4.03	3.98	187.85	Low	Jixi	Heilongjiang, China	Large amounts of fault structures	Zhang et al. [45]
No. 21	10.41	2.73	2.01	267.32	Low	Pingdingshan	Henan, China	A series of faults and folds existence	Su et al. [48]
No. 22	9.08	3.51	2.26	368.00	Low	Chengjiao	Henan, China	Wide and gentle slope fold structures accompanied by a number of faults	Su et al. [23]
No. 23	8.67	2.97	2.62	110.45	Low	Pingdingshan	Henan, China	A series of faults and folds existence	Su et al. [48]
No. 24	6.87	2.48	0.64	548.20	None	Pingdingshan	Henan, China	A series of faults and folds existence	Su et al. [48]
No. 25	6.64	1.99	1.88	517.06	None	Chengjiao	Henan, China	Wide and gentle slope fold structures accompanied by a number of faults	Su et al. [23]
No. 26	6.07	0.89	1.29	514.40	None	Chengjiao	Henan, China	Wide and gentle slope fold structures accompanied by a number of faults	Su et al. [23]
No. 27	4.98	1.02	1.23	426.13	None	Chengjiao	Henan, China	Wide and gentle slope fold structures accompanied by a number of faults	Su et al. [23]

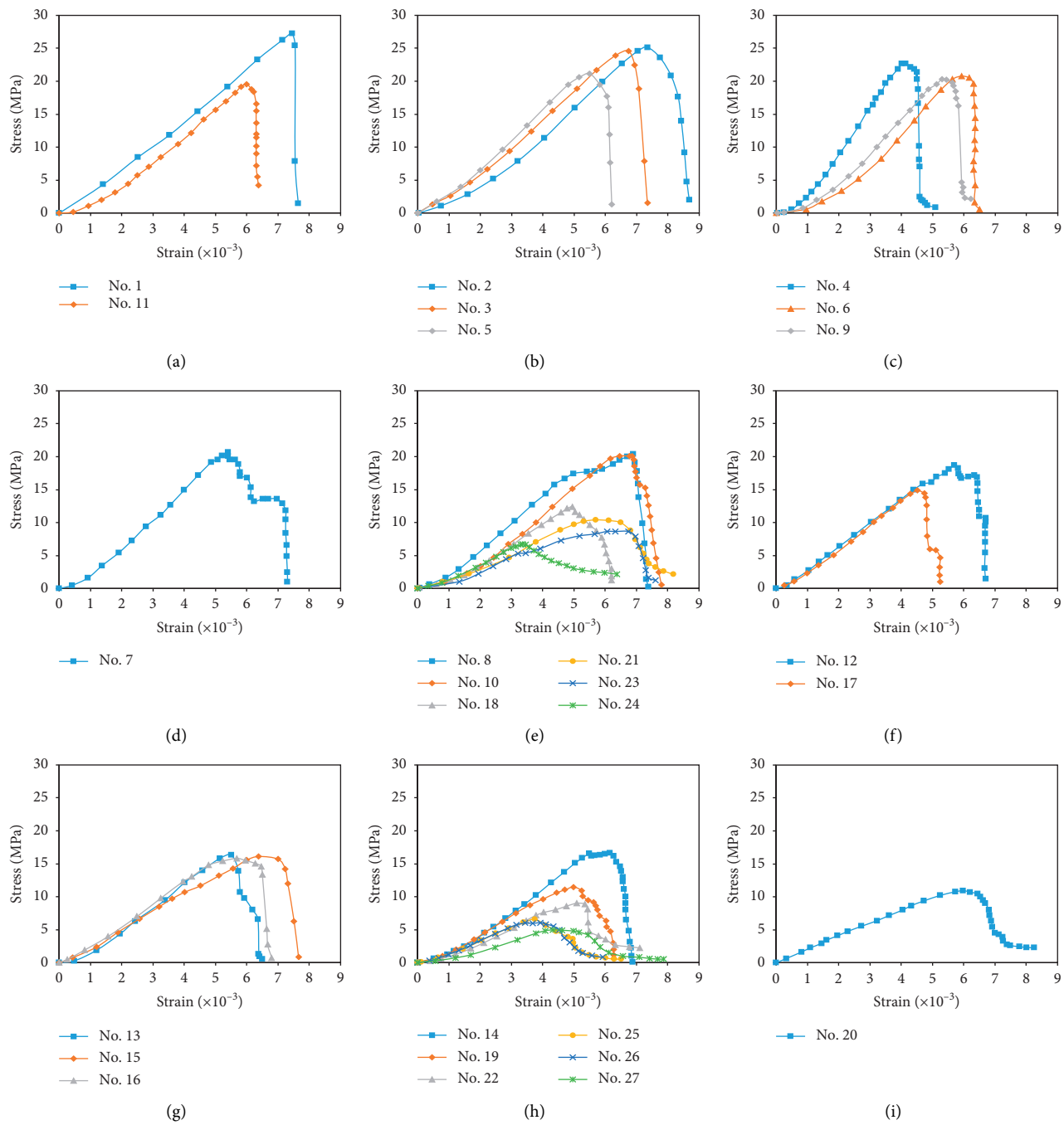

Figure 2: The stress-strain curves of 27 coal specimens grouped based on coal mines where they are taken: (a) Zhaogu coal mine; (b) Tangshan coal mine; (c) Mentougou coal mine; (d) Sanjiaohe coal mine; (e) Pingdingshan coal mine; (f) Zhangcun coal mine; (g) Qianqiu coal mine; (h) Chengjiao coal mine; (i) Jixi coal mine.

known as the determination coefficient) R^2, and the distribution interval is (0, 1). The larger the R^2 is, the better the fitting degree is:

$$R^2 = \frac{\mathrm{SSR}}{\mathrm{SST}} = 1 - \frac{\mathrm{SSE}}{\mathrm{SST}}, \tag{1}$$

where SSR is the sum of squares of regression, SSE is the sum of squares of residuals, and SST is the sum of squares of total deviations. The calculation formula of R^2 is further derived, and the results are as follows:

$$R^2 = 1 - \frac{\sum_{i=1}^{n} (\hat{y}_i - \overline{y})^2}{\sum_{i=1}^{n} (y_i - \overline{y})^2}, \tag{2}$$

where y_i is the real observation value, the stress value of the test curve is substituted in the calculation, $\overline{y}$ is the average value of the real observation, the average value of the stress value of the selected test curve is substituted in the calculation, $\hat{y}$ is the fitting value, and the stress value of the curve obtained by numerical fitting is substituted in the calculation.

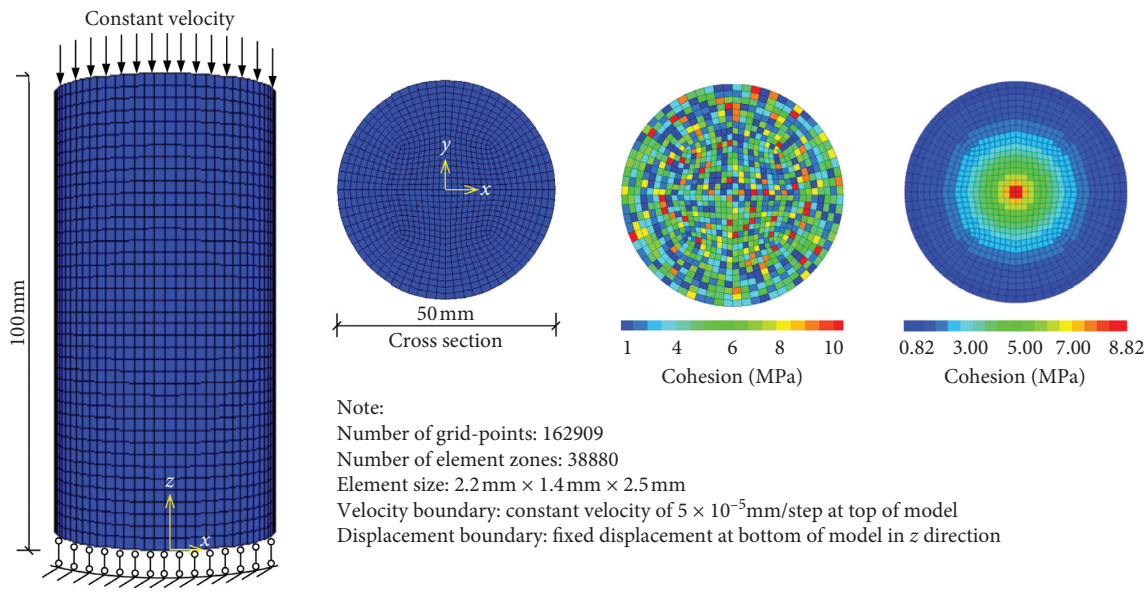

Figure 3: Numerical model of coal specimen and the uniaxial compressive boundary condition.

Table 3: Empirical parameters initially used in the numerical simulation [51].

UCS (MPa)	Young's modulus (GPa)	Poisson's ratio	Cohesion (MPa)	Friction angle (°)	Tensile strength (MPa)
4.90–10.0	0.29–2.45	0.1–0.30	0.98–9.81	19–40	0.24–5.79
9.81–15.7	2.45–6.37	0.1–0.30	1.96–3.92	28–35	1.47–2.45
19.6–49.0	8.83–22.60	0.1–0.35	3.92–5.88	35–45	1.96–9.81

It is revealed that numerical fitted stress-strain curves can be used to study the mechanical parameters of coal specimens as most of fitting coefficients R^2 between test and numerical results are greater than 98%. To calculate the dissipated plastic energy before 80–90% of the coal peak strength, Figure 4 presents the unload stress-strain curve. Table 4 lists the numerical parameters determined by numerically fitting the 27 stress-strain curves in the uniaxial compressive test. In the process of fitting, we find that the elastic modulus affects the time of the peak value appears. The larger the elastic modulus is, the earlier the peak value of the curve appears, the cohesion affects the peak value of the curve, the higher the cohesion, the greater the peak strength of the curve, and the friction angle affects the peak strength and the postpeak section of the curve. The larger the friction angle, the greater the peak value of the curve and the greater the brittleness of the postpeak segment is. Tensile strength and Poisson's ratio have little influence on the curve. According to the data in Table 4, when the uniaxial compressive strength changes from 27.26 MPa to 4.98 MPa, the cohesion changes from 6.82 MPa to 1.19 MPa, and the change amplitude is the most obvious among all the parameters. Therefore, the remaining parameters are regarded as constants, ignoring the influence of these parameters on bursting proneness. It should be pointed out that in this paper, No. 7 and No. 8 coal are determined as high bursting proneness according to R_C, W_{ET}, and K_E indexes, and low bursting proneness according to D_t indexes; No. 16 and No. 17 coal are determined as bursting proneness according to R_C and W_{ET} indexes, and low impact tendency according to K_E and D_t indexes. There are still similar problems in the data in the table, which are not listed here one by one. Therefore, the existing identification index has the problem of inconsistent identification results.

As shown in Figure 1, the bursting proneness indices are calculated by the area under the stress-strain curves. It can be seen from Figure 4 that the prepeak strength curves, postpeak strength curves, and the unload curves are approximately regarded as linear lines. To list these three linear equations for 27 specimens, the No. 12 coal specimen is taken as an example to approximately present, as shown in Figure 5.

In this study, the functional equations of these three curves can be assumed as

$$\begin{aligned} y &= E_1 x, \\ y &= E_2 x - b_2, \\ y &= -E_3 x + b_3, \end{aligned} \tag{3}$$

respectively, and the parameters of E_1, E_2, E_3, b_2, and b_3 are the slope and intercept of these three linear curves. By calculating the fitted stress-strain curves, the values of slope and intercept for the 27 coal specimens are listed in Table 5. In this table, the UCS of coal specimens is listed as well.

Figure 6 shows the relation between the parameters of E_1, E_2, E_3, and the UCS. It is revealed that the E_1 and E_2 approximately increase linearly with the increase of the UCS while an exponential relation between E_3 and UCS can be

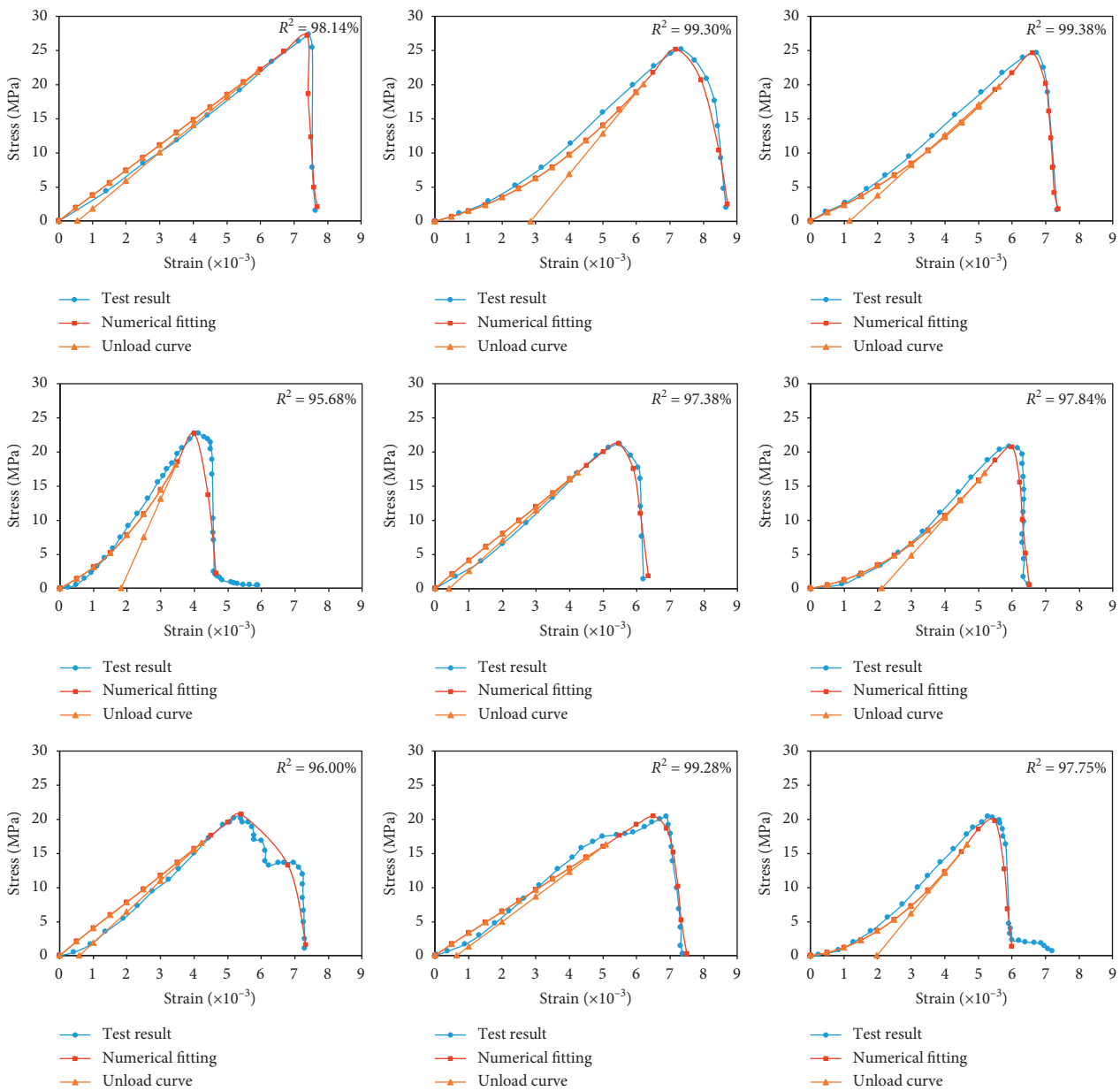

(a)

Figure 4: Continued.

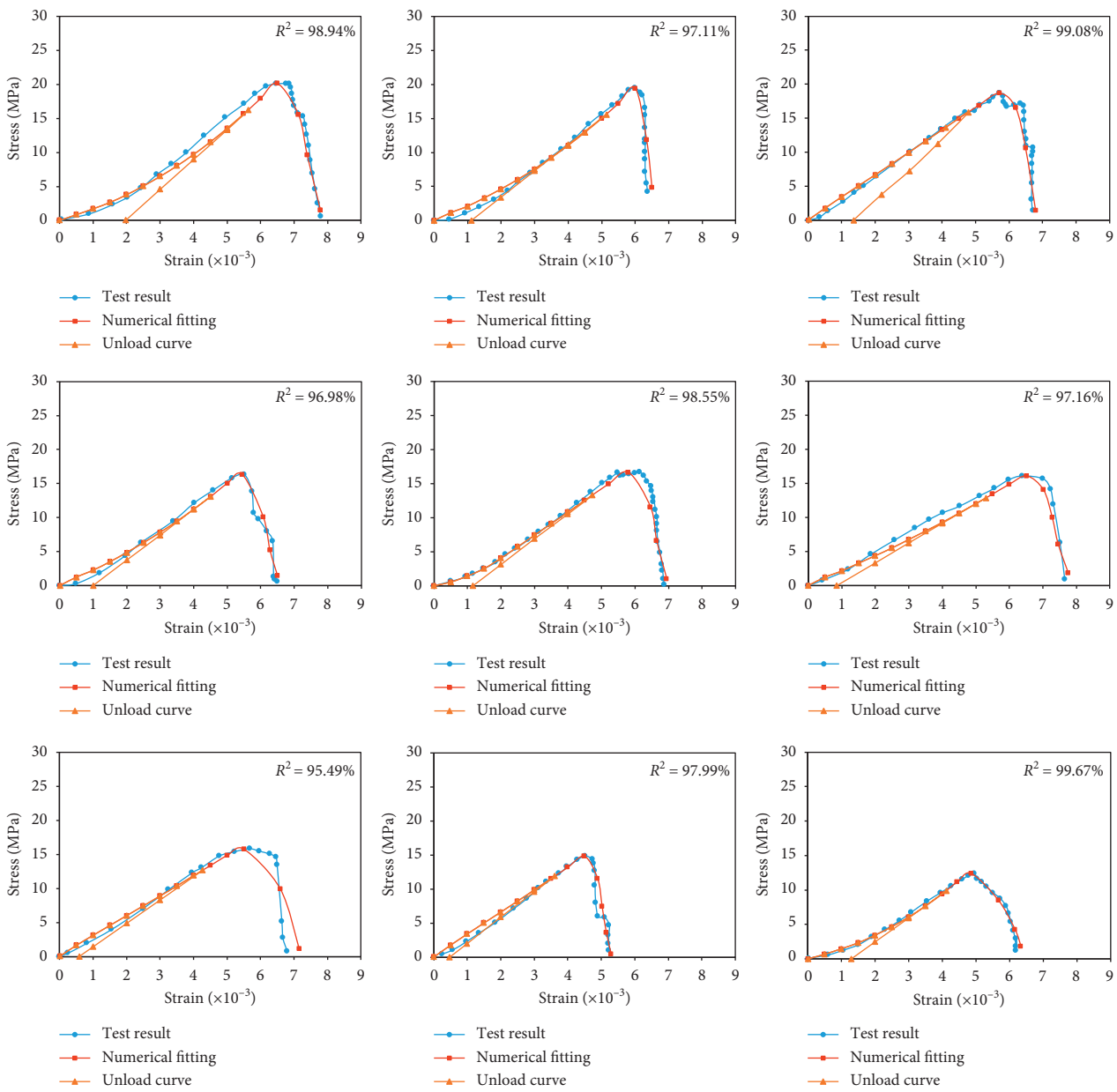

(b)

Figure 4: Continued.

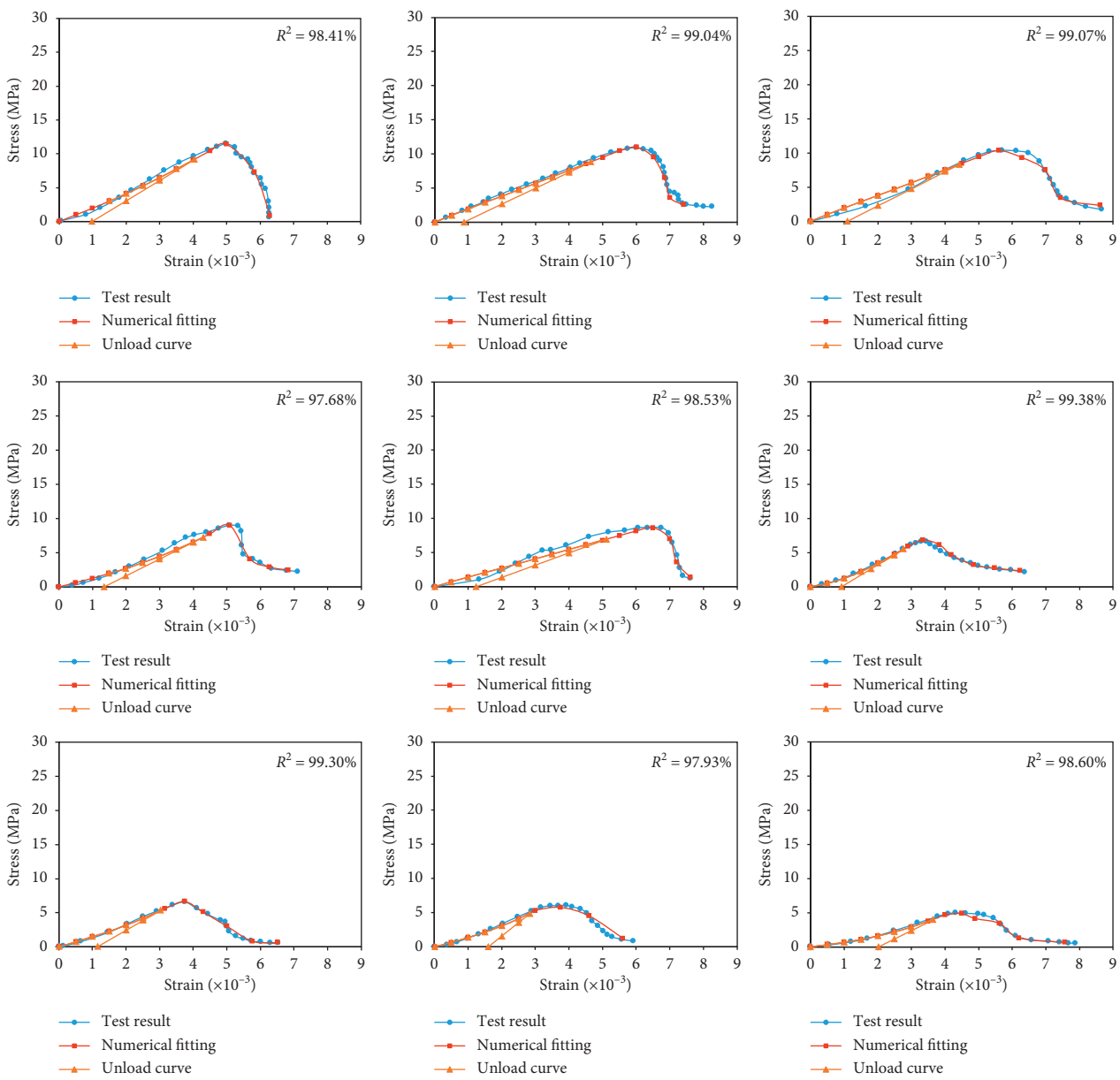

(c)

Figure 4: Numerical fitted stress-strain and unload curves of the 27 coal specimens by the uniaxial compressive test: (a) No .1 to No. 9 coal specimens. (b) No. 10 to No. 18 coal specimens. (c) No. 19 to No. 27 coal specimens.

assumed. Therefore, the relational equation between the parameters of E_1, E_2, E_3, and UCS can be assumed as

$$E_1 = k_1 R_c + e_1, \tag{4}$$

$$E_2 = k_2 R_c + e_2, \tag{5}$$

$$E_3 = k_3 R_c^{e_3}, \tag{6}$$

where k_1, k_2, k_3, e_1, e_2, and e_3 are constant coefficients of these three equations; R_c is the UCS of coal specimens.

According to the coefficients of curves in Figure 5, the intercepts of unload and postpeak strength curves are, respectively,

$$b_2 = \left(\frac{E_2}{E_1} - 1\right) n R_c, \tag{7}$$

$$b_3 = \left(1 + \frac{E_3}{E_1}\right) R_c, \tag{8}$$

where the parameter n is a ratio between 80% and 90% of the peak strength of coal.

According to the numerical parameters of these coal specimens in Table 4 and corresponding bursting proneness indices in Table 2, Figure 7 is drawn to study the relationship between the bursting proneness indices and cohesion and to reveal the effectiveness of coal properties on the bursting

Table 4: The mechanical parameters determined by numerically fitting the stress-strain curve in the uniaxial compressive test.

Specimens	Young's modulus (GPa)	Poisson's ratio	UCS (MPa)	Cohesion			Friction angle			Tensile strength		
				Original value (MPa)	Softening rate (%)	Residual value (MPa)	Original value (°)	Softening rate (%)	Residual value (°)	Original value (MPa)	Softening rate (%)	Residual value (MPa)
No. 1	3.69	0.22	27.26	6.82	0.20	1.00	37	0.20	35	2.87	0.20	0
No. 2	3.50	0.22	25.13	6.20	5.20	0.30	37	5.20	35	2.89	5.20	0
No. 3	3.65	0.22	24.58	6.07	2.80	0.50	37	2.80	35	2.43	2.80	0
No. 4	3.58	0.22	22.70	5.58	1.80	1.50	37	1.80	35	2.43	1.80	0
No. 5	3.93	0.22	21.24	5.25	4.15	0.30	37	4.15	33	2.16	4.15	0
No. 6	3.57	0.22	21.08	4.73	2.10	0.51	41	2.10	39	2.18	2.10	0
No. 7	3.82	0.23	20.68	5.10	7.00	0.50	37	7.00	35	2.21	7.00	0
No. 8	3.15	0.22	20.39	5.05	4.70	0.50	37	4.70	35	2.20	4.70	0
No. 9	3.81	0.22	20.33	5.02	2.15	0.50	37	2.15	35	2.10	2.15	0
No. 10	3.08	0.22	20.24	4.98	4.05	1.50	37	4.05	35	2.03	4.05	0
No. 11	3.22	0.22	19.53	4.81	1.20	0.50	38	1.20	35	2.07	1.20	0
No. 12	3.27	0.25	18.65	4.82	5.00	0.30	35	5.00	31	1.91	5.00	0
No. 13	3.02	0.22	16.71	4.02	3.50	0.50	37	3.50	35	1.78	3.50	0
No. 14	2.86	0.22	16.65	4.10	4.20	0.10	37	4.20	35	2.02	4.20	0
No. 15	2.47	0.22	16.09	3.97	4.32	0.50	37	4.32	35	1.77	4.32	0
No. 16	2.90	0.22	15.82	3.89	5.80	0.28	37	5.80	35	1.53	5.80	0
No. 17	3.24	0.25	14.88	3.85	2.40	0.30	35	2.40	31	1.54	2.40	0
No. 18	2.56	0.23	12.40	3.03	3.50	0.50	35	3.50	32	1.24	3.50	0
No. 19	2.33	0.28	11.46	3.63	5.70	0.10	25	5.70	22	1.18	5.70	0
No. 20	1.87	0.24	11.03	3.10	5.00	0.60	31	5.00	27	1.14	5.00	0
No. 21	1.83	0.24	10.41	2.79	7.50	0.15	33	7.50	29	1.01	7.50	0
No. 22	1.78	0.27	9.08	2.20	1.90	0.80	35	1.90	31	0.93	1.90	0
No. 23	1.34	0.25	8.67	2.39	4.50	0.30	32	4.50	28	0.89	4.50	0
No. 24	2.02	0.22	6.87	1.66	2.50	0.20	37	2.50	35	0.75	2.50	0
No. 25	1.78	0.22	6.64	1.47	3.20	0.01	41	3.20	39	0.70	3.20	0
No. 26	1.77	0.22	6.07	1.46	4.00	0.01	37	4.00	35	0.67	4.00	0
No. 27	1.16	0.22	4.98	1.19	3.55	0.10	37	3.55	35	0.55	3.55	0

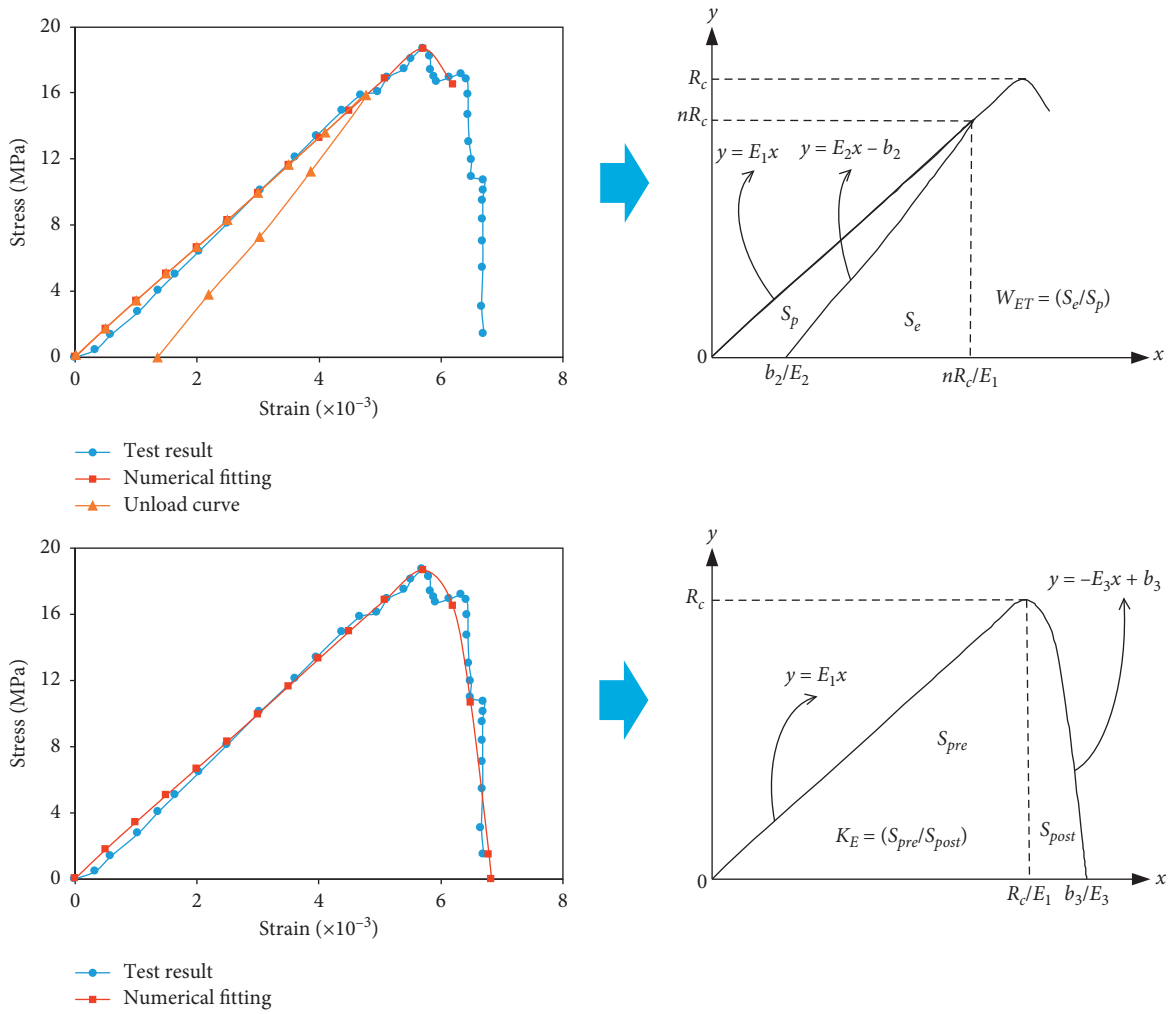

Figure 5: The functional equations of stress-strain curve before peak strength, the unload curve before 80–90% of peak strength, and the curve after peak strength for No. 12 coal specimen.

proneness of coal. In addition, the theoretical relation between bursting proneness indices and cohesion is deduced for comparison with the numerical results, as shown in Figure 7. The two dash lines in these figures are drawn to represent the minimum boundary of high bursting proneness (red lines) and minimum boundary of low bursting proneness (orange lines).

3.3. Relation between Index R_c and Cohesion. Figure 7(a) presents the relation between bursting proneness index R_c and cohesion. It is revealed that the index R_c linearly increases with the increase of cohesion. According to the theory of Mohr–Coulomb criterion, the UCS or index R_c is related to cohesion and friction angle by

$$R_c = \frac{2C\cos\varphi}{1-\sin\varphi}, \tag{9}$$

where C is cohesion and φ is friction angle of coal specimens.

According to equation (9), if the friction angle φ is constant, the theoretical linear relation between cohesion and index R_c can be obtained. Theoretical and numerical results are in good agreement, as shown in Figure 7(a). In addition, it also can be seen that coal is of high bursting proneness when its cohesion is approximately greater than 3.5 MPa and it is of low bursting proneness when the cohesion is approximately greater than 2.0 MPa.

3.4. Relation between Index W_{ET} and Cohesion. Figure 7(b) presents the relation between bursting proneness index W_{ET} and cohesion. It can be seen from the numerical results that the index W_{ET} approximately linearly increases with the increase of cohesion.

According to the current standard in China, the index W_{ET} is calculated as a ratio of the elastic energy accumulated and the dissipated plastic energy before 80–90% of the coal peak strength [17]. As shown in Figures 1 and 5, elastic energy accumulated (S_e) and the dissipated plastic energy (S_p) before 80–90% of the peak strength are calculated as

Table 5: Parameters of E_1, E_2, and E_3 of stress-strain curve before peak strength, unload curve before 80–90% of peak strength, and curve after peak strength of the 27 coal specimens.

Specimens	E_1	E_2	E_3	UCS (MPa)
No. 1	3.69	4.80	79.02	27.26
No. 2	3.50	4.24	73.12	25.13
No. 3	3.65	4.43	70.35	24.58
No. 4	3.58	6.67	55.33	22.70
No. 5	3.93	4.43	50.13	21.24
No. 6	3.57	4.32	35.16	21.08
No. 7	3.82	4.53	30.65	20.68
No. 8	3.15	3.66	35.93	20.39
No. 9	3.81	4.58	28.33	20.33
No. 10	3.08	3.73	27.63	20.24
No. 11	3.22	3.86	22.37	19.53
No. 12	3.27	3.74	21.66	18.65
No. 13	3.02	3.73	20.98	16.71
No. 14	2.86	3.73	14.99	16.65
No. 15	2.47	2.89	20.27	16.09
No. 16	2.90	3.43	18.17	15.82
No. 17	3.24	3.79	15.09	14.88
No. 18	2.56	3.51	14.20	12.40
No. 19	2.33	3.00	13.72	11.46
No. 20	1.87	2.34	10.52	11.03
No. 21	1.83	2.50	5.02	10.41
No. 22	1.78	2.46	3.37	9.08
No. 23	1.34	2.32	5.53	8.67
No. 24	2.02	2.98	1.56	6.87
No. 25	1.78	2.84	1.80	6.64
No. 26	1.77	2.62	2.49	6.07
No. 27	1.16	2.46	1.97	4.98

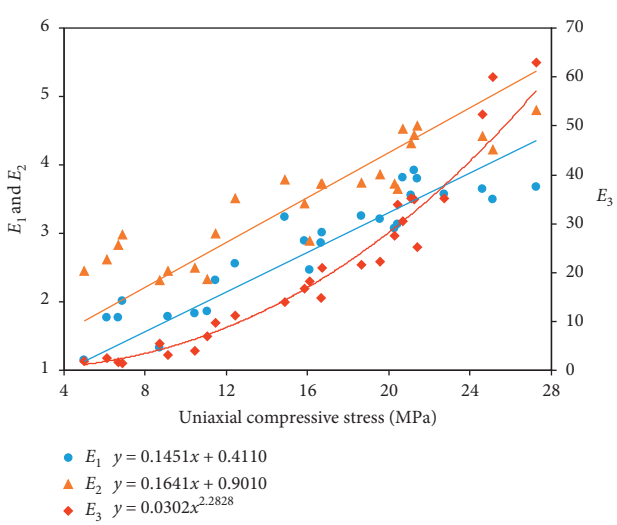

Figure 6: The variation of E_1, E_2, and E_3 versus the UCS of 27 coal specimens.

$$S_e = \int_{b_2/E_2}^{nR_c/E_1} (E_2 x - b_2)\mathrm{d}x = \frac{1}{2}\left(\frac{nR_c}{E_1} - \frac{b_2}{E_2}\right) nR_c, \tag{10}$$

$$S_p = \int_0^{nR_c/E_1} E_1 x \mathrm{d}x - \int_{b_2/E_2}^{nR_c/E_1} (E_2 x - b_2)\mathrm{d}x = \frac{1}{2}\frac{b_2}{E_2} nR_c. \tag{11}$$

Substituting equations (4), (5), and (7) into equations (10) and (11), then the index W_{ET} is calculated as

$$W_{ET} = \frac{S_e}{S_p} = \frac{E_2}{E_1 b_2} nR_c - 1 = \frac{E_1}{E_2 - E_1} = \frac{k_1 R_c + e_1}{(k_2 - k_1)R_c + (e_2 - e_1)}. \tag{12}$$

Substitution of equation (9) into equation (12) gives the relation between index W_{ET} and cohesion as

$$W_{ET} = \frac{2Ck_1 \cos\varphi + e_1(1 - \sin\varphi)}{2C(k_2 - k_1)\cos\varphi + (e_2 - e_1)(1 - \sin\varphi)}. \tag{13}$$

Therefore, if the friction angle φ is constant, an approximate linear relation between index W_{ET} and cohesion holds. This theoretical relation is identical with the numerical results, as shown in Figure 7(b). It also can be revealed that a specimen is of the high bursting proneness when its cohesion is greater than 3.5 MPa and the low bursting proneness is regarded when the cohesion is approximately greater than 1.5 MPa.

3.5. Relation between Index K_E and Cohesion. Figure 7(c) presents the relation between bursting proneness index K_E and cohesion. It can be seen that the index K_E increases with the increase of cohesion. The index K_E gradually increases as the cohesion increases from 1.5 to 3.5 MPa, and then it

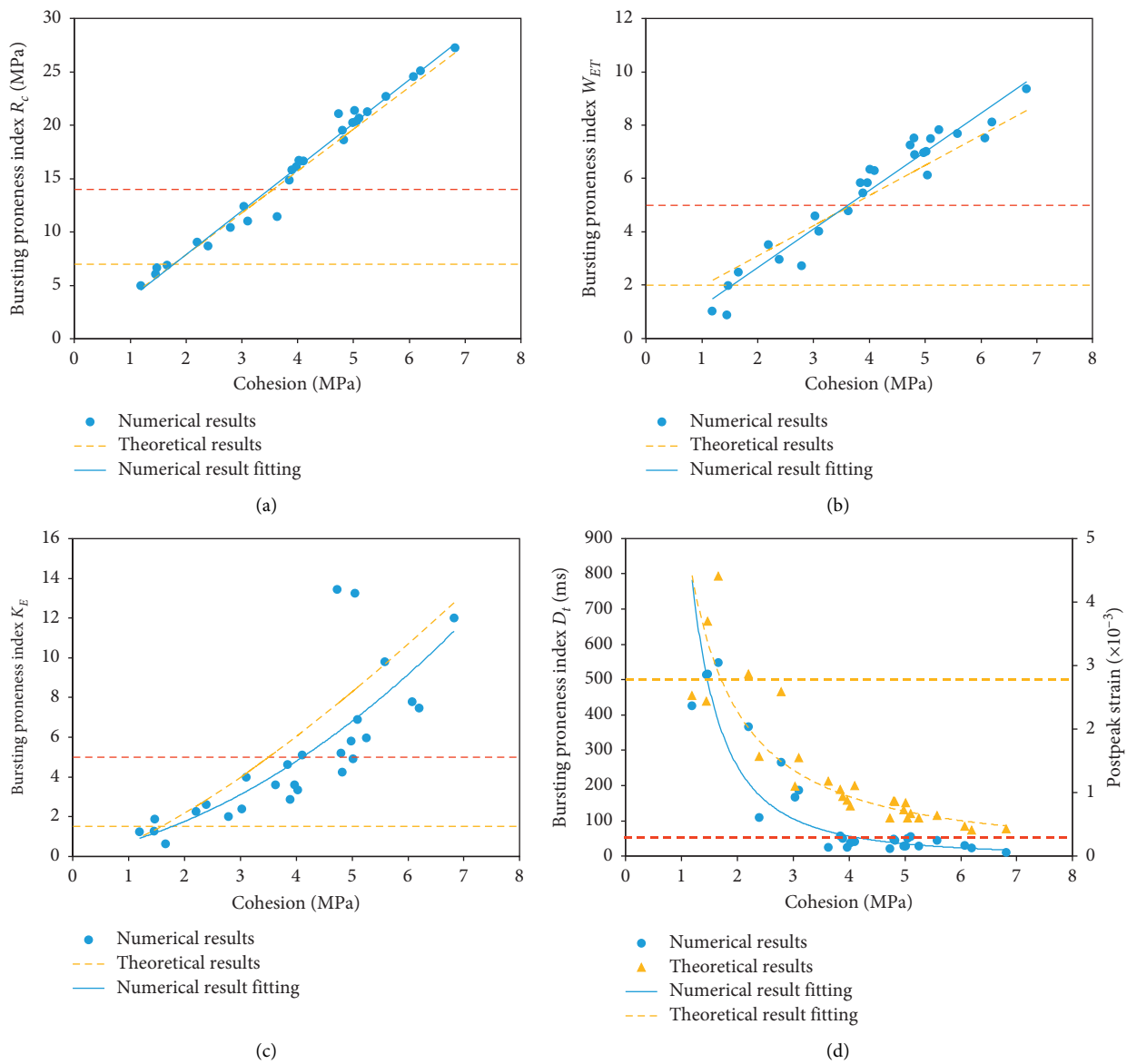

FIGURE 7: The relationship between bursting proneness indices and cohesion: (a) Index R_c (UCS). (b) Index W_{ET}. (c) Index K_E (d) Index D_t and postpeak strain.

sharply increases when the cohesion is greater than 3.5–4.0 MPa.

According to the current standard in China, the bursting energy index (K_E) (Figure 1(b)) is a ratio of the strain energy accumulated before peak strength and the strain energy released after peak strength [17]. As shown in Figures 1 and 5, strain energy accumulated before peak strength (S_{pre}) and strain energy released after peak strength (S_{post}) are, respectively, calculated with equations (14) and (15) as

$$S_{\text{pre}} = \int_0^{R_c/E_1} E_1 x \mathrm{d}x = \frac{R_c^2}{2E_1}, \tag{14}$$

$$S_{\text{post}} = \int_{R_c/E_1}^{b_3/E_3} (-E_3 x + b_3)\mathrm{d}x = \frac{1}{2}\left(\frac{b_3}{E_3} - \frac{R_c}{E_1}\right)R_c. \tag{15}$$

Substituting equations (4), (6), and (8) into equations (14) and (15), then the index K_E is calculated as

$$K_E = \frac{S_{\text{pre}}}{S_{\text{post}}} = \frac{R_c/E_1}{(b_3/E_3) - (R_c/E_1)} = \frac{E_3}{E_1} = \frac{k_3 R_c^{e_3}}{k_1 R_c + e_1}. \tag{16}$$

Substitution of equation (9) into equation (16) gives the relation between index K_E and cohesion as

$$K_E = \frac{k_3 (2C\cos\varphi)^{e_3}}{2k_1 C\cos\varphi (1 - \sin\varphi)^{e_3 - 1} + e_1 (1 - \sin\varphi)^{e_3}}. \tag{17}$$

If the friction angle φ is constant, a power functional relation between index K_E and cohesion is obtained. This theoretical relation is consistent with the numerical results, as shown in Figure 7(c). It also can be seen that the high bursting proneness is warranted when the cohesion is

approximately greater than 4.0 MPa and the low bursting proneness is assumed when the cohesion is approximately greater than 1.5 MPa.

3.6. Relation between Index D_t and Cohesion. Figure 7(d) presents the relation between bursting proneness index D_t and cohesion. It can be seen that the index D_t decreases with the increase of cohesion. The index D_t sharply decreases when the cohesion increases from 1.5 to 3.5 MPa while it gradually decreases when the cohesion is over 3.5–4.0 MPa.

According to Figure 1, the postpeak strain and dynamic fracturing duration (D_t) are equivalent to illustrate the span from peak strength to complete failure of coal specimen. Therefore, the dynamic fracturing duration (D_t) can be replaced by the postpeak strain in this part to study the relation between index D_t and cohesion. The postpeak strain can be calculated as

$$\varepsilon_{\text{post}} = \frac{R_c}{E_3} = \frac{1}{k_3 R_c^{e_3-1}}. \tag{18}$$

Substitution of equation (9) into equation (18) gives the relation between postpeak strain and cohesion as

$$\varepsilon_{\text{post}} = \frac{R_c}{E_3} = \frac{(1-\sin\varphi)^{e_3-1}}{k_3 (2C\cos\varphi)^{e_3-1}}. \tag{19}$$

If the friction angle φ is constant, a power functional relation between the postpeak strain and cohesion can be obtained, which is found to be in good agreement with the numerical results, as shown in Figure 7(d). It also can be seen that the specimen is of high bursting proneness when the cohesion is approximately greater than 4.0 MPa and the low bursting proneness is reached when the cohesion is greater than 1.5 MPa.

4. Numerical Simulation of Coal Heterogeneity

4.1. Numerically Assignment of Nonuniform Distribution of Coal Parameter. Coal heterogeneity is a major factor to influence its mechanical behaviors, such as the UCS, shear strength, failure behavior, crack evolution, and bursting proneness [39, 52–56]. Probability distribution is a widely used method to statistically describe the distribution in mechanical properties of materials and analyze the characteristics of rock and coal heterogeneity.

In this study, the influence of nonuniform distribution of cohesion on the coal strength (UCS) is mainly analyzed. Eight types of probability distribution functions are employed to assignment cohesion to the numerical model. Table 6 lists these eight probability density functions and their relative parameters such as mathematical expectation, variance, and standard deviation. The mathematical expectation can be approximately regarded as the average value, and standard deviation is a parameter to represent the scatter degree of cohesion in the numerical model. The greater the standard deviation is, the larger the scatter degree of cohesion in the numerical model will be.

The No. 12 coal specimen is taken again as an example in this part. The cohesion of this specimen is 4.82 MPa under homogeneous conditions, as listed in Table 4. The cohesion of 4.82 MPa could be set as the average value and can be regarded as the mathematical expectation. Then, eight intervals of cohesion with decreasing scatter degree are selected, including 0.82–8.82 MPa, 1.32–8.32 MPa, 1.82–7.82 MPa, 2.32–7.32 MPa, 2.82–6.82 MPa, 3.32–6.32 MPa, 3.82–5.82 MPa, and 4.32–5.32 MPa. Table 7 lists the standard deviation of the probability distributions for these eight intervals.

Since the coal specimen is an axisymmetric cylinder which is obtained by laboratory drilling, the strength of the specimen center is generally greater than that of the specimen edge. Therefore, nonuniform cohesion will be assigned to the numerical model from the center to edge of cross section according to the above eight distribution functions. Figure 8 shows the nonuniform cohesion assignment results in coal specimen under the eight cohesion scatter intervals. In these figures, the curves reflect the cohesion variation in the model cross section from center to edge while the contours present the distribution of cohesion in the cross section.

4.2. Influence of Scatter Degree of Cohesion on the UCS. Since the UCS is one of the indices to evaluate the bursting proneness of coal, it is selected to study the bursting proneness in this part. Figure 9 presents the stress-strain curves of No. 12 coal specimen under nonuniform cohesion distribution in the model. In these figures, the stress-strain curve under the uniform assignment of cohesion is also drawn to analyze the differences between the homogeneous and heterogeneous mechanical characteristics. It can be seen that the UCS decreases with the increasing of scatter degree. All of the stress-strain curves suggest that the UCS of coal specimen with nonuniform cohesion is lower than that of homogeneous coal. With the decreasing of cohesion scatter degree, the stress-strain curve of coal specimen is more and more close to the stress-strain curve under homogeneous condition. In addition, the stress-strain curves of coal specimen are getting closer and closer to each other with the decreasing of cohesion scatter degree. However, the relationship between the UCS and cohesion scatter degree is not linear. To in-depth study their relationships, Figure 10 presents the numerical results of UCS under the different standard deviations for eight probability distributions. In this figure, it is revealed that the UCS nonlinearly decreases with the increasing standard deviation. The greater the standard deviation is, the larger the scatter degree of cohesion in the numerical model will be. Therefore, the UCS of coal specimen will nonlinearly decrease with the increasing of cohesion scatter degree. In other words, UCS of coal specimen will decrease rapidly with the increasing of cohesion scatter degree. Since USC is a bursting proneness index, the coal bursting proneness will decrease with the increasing of cohesion scatter degree. The larger the cohesion scatter degree increase is, the lower the bursting proneness will be.

Table 6: Eight probability density functions employed to simulate the heterogeneous distribution of cohesions in the numerical model.

Distribution	Probability density function ($x > 0$)	Mathematical expectation	Variance	Standard deviation
Weibull	$f(x) = (m/x_0)(x/x_0)^{m-1}e^{-(x/x_0)^m}$	$x_0\Gamma((1/m)+1)$	$x_0^2\left\{\Gamma((2/m)+1) - [\Gamma((1/m)+1)]^2\right\}$	$x_0\sqrt{\left\{\Gamma((2/m)+1) - [\Gamma((1/m)+1)]^2\right\}}$
Normal	$f(x) = (1/\sqrt{2\pi}\,\sigma)e^{-((x-\mu)^2/(2\sigma^2))}$	μ	σ^2	σ
Rayleigh	$f(x) = (x/\sigma^2)e^{-(x^2/(2\sigma^2))}$	$\sqrt{\pi/2}\sigma$	$((4-\pi)/2)\sigma^2$	$\sqrt{(4-\pi)/2}\sigma$
Chi-square	$f(x) = \frac{1}{2^{n/2}\Gamma(n/2)}x^{(n/2)-1}e^{-(x/2)}$	n	$2n$	$\sqrt{2n}$
Student's	$f(x) = (\Gamma[(n+1)/2]/\sqrt{n\pi}\,\Gamma(n/2))(1+(x^2/n))^{-((n+1)/2)}$	0	$(n/(n-2))$, $n > 2$	$\sqrt{(n/(n-2))}$, $n > 2$
Exponent	$f(x) = (1/\lambda)e^{-(x/\lambda)}$	λ	λ^2	λ
Cauchy	$f(x) = (1/\pi)(\lambda/(\lambda^2+(x-a)^2))$	—	—	—
Fisher	$f(x) = (\Gamma[(n_1+n_2)/2](n_1/n_2)((n_1/n_2)x)^{(n_1/2)-1} / \Gamma(n_1/2)\Gamma(n_2/2)(1+(n_1/n_2)x)^{(n_1+n_2)/2})$	$(n_2/(n_2-2))$, $n_2 > 2$	$(2n_2^2(n_1+n_2-2)/n_1(n_2-2)^2(n_2-4))$, $n_2 > 4$	$(n_2/(n_2-2))\sqrt{2(n_1+n_2-2)/n_1(n_2-4)}$, $n_2 > 4$

Table 7: Values of standard deviation of the eight probability distributions under eight cohesion scatter intervals.

Distribution	Cohesion intervals (MPa)							
	0.82–8.82	1.32–8.32	1.82–7.82	2.32–7.32	2.82–6.82	3.32–6.32	3.82–5.82	4.32–5.32
Weibull	2.78	2.39	2.02	1.66	1.31	0.98	0.64	0.32
Normal	2.79	2.41	2.05	1.69	1.34	0.99	0.66	0.33
Rayleigh	2.57	2.24	1.91	1.58	1.26	0.94	0.62	0.31
Chi-square	2.64	2.32	2.00	1.66	1.33	0.99	0.66	0.33
Student's	2.77	2.41	2.06	1.70	1.35	1.00	0.66	0.33
Exponent	2.27	2.02	1.75	1.47	1.19	0.89	0.60	0.30
Cauchy	2.56	2.33	2.03	1.70	1.35	1.01	0.67	0.33
Fisher	2.38	2.18	1.91	1.62	1.31	0.99	0.66	0.33

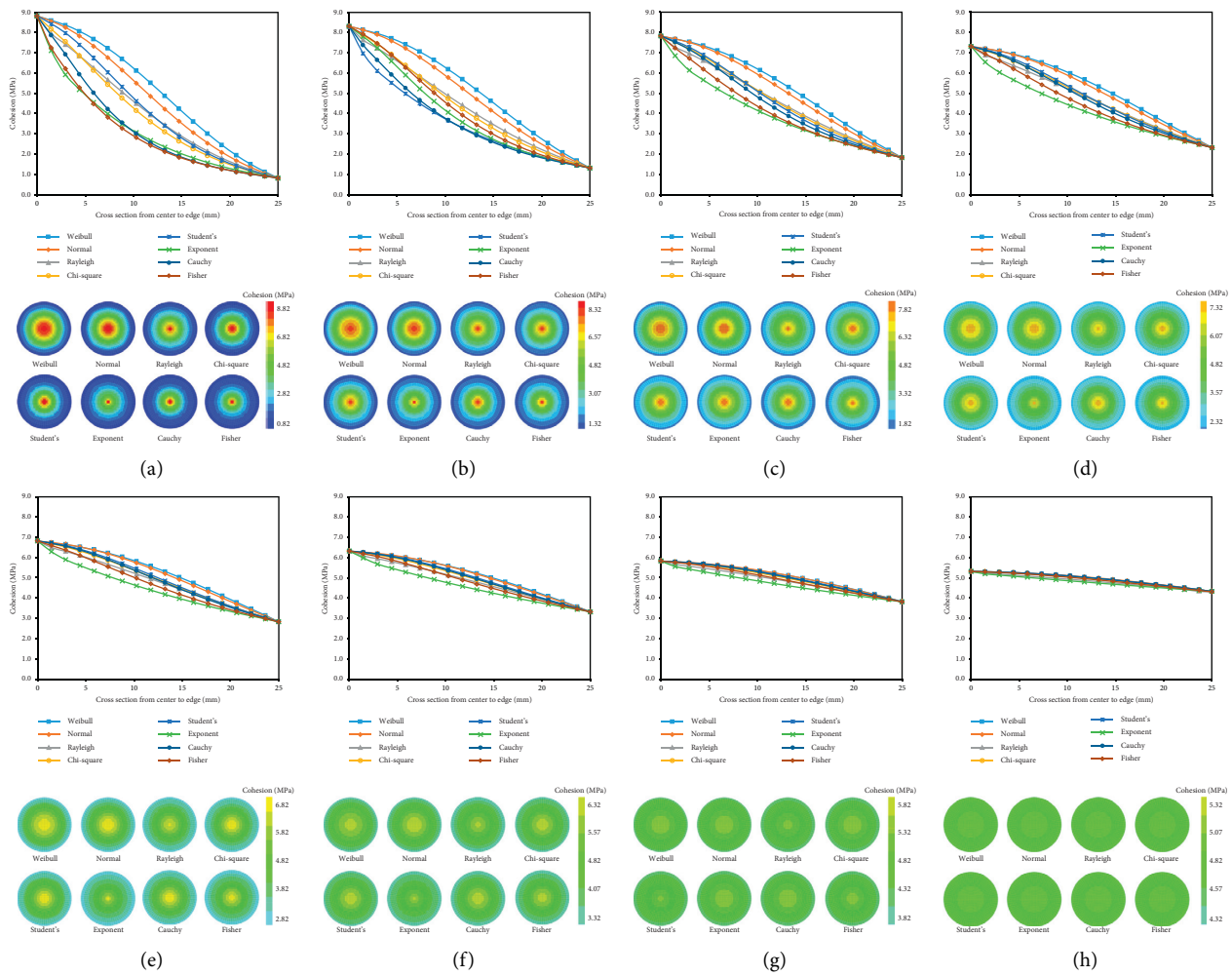

Figure 8: Nonuniform cohesion assignment results in coal specimen under eight cohesion scatter intervals: (a) cohesion interval of 0.82–8.82 MPa, (b) cohesion interval of 1.32–8.32 MPa, (c) cohesion interval of 1.82–7.82 MPa, (d) cohesion interval of 2.32–7.32 MPa, (e) cohesion interval of 2.82–6.82 MPa, (f) cohesion interval of 3.32–6.32 MPa, (g) cohesion interval of 3.82–5.82 MPa, and (h) cohesion interval of 4.32–5.32 MPa.

In addition, as shown in Figure 10, different probability distributions describe different effects of nonuniform cohesion on the UCS of coal specimen. In these eight probability distributions, with the increasing of cohesion scatter degree, the UCS decrement of coal specimen assigned by Weibull and Normal distributions was smaller than that by the other six distributions. The UCS of coal specimen assigned by Fisher distribution decreases fastest among these eight distributions with the increasing of cohesion scatter degree. It is important to note that these eight probability functions employed in this study are the most commonly used distributions to describe the heterogeneous coal. The

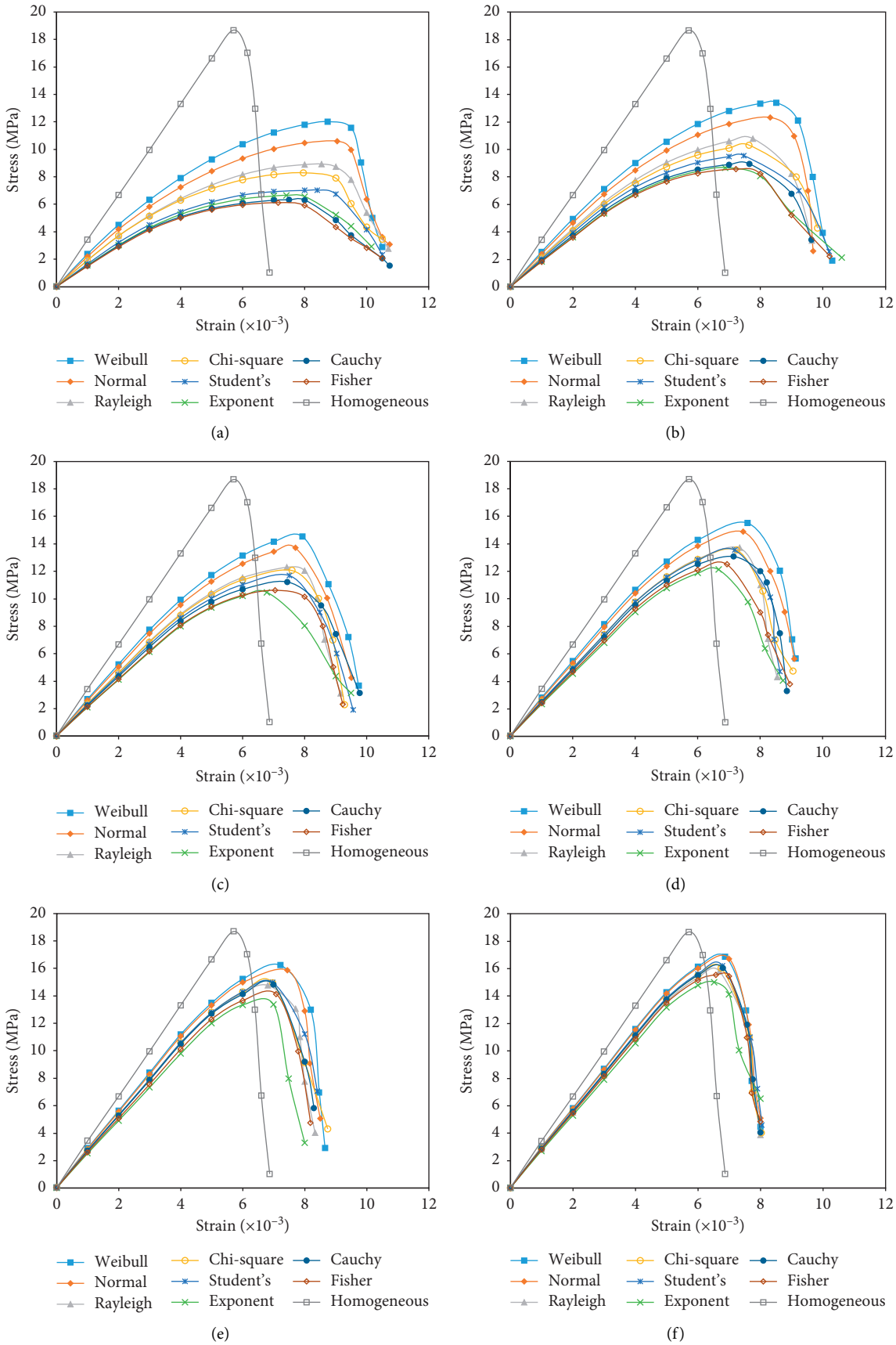

Figure 9: Continued.

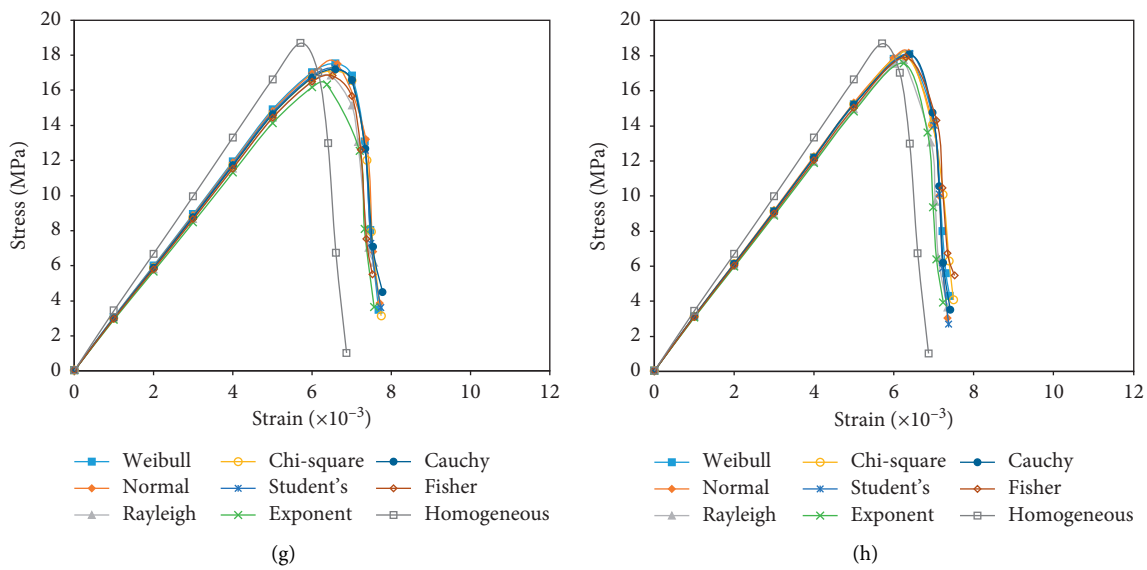

Figure 9: Stress-strain curves of No. 12 coal specimen under nonuniform cohesion distribution in the model with eight different scatter intervals: (a) cohesion interval of 0.82–8.82 MPa, (b) cohesion interval of 1.32–8.32 MPa, (c) cohesion interval of 1.82–7.82 MPa, (d) cohesion interval of 2.32–7.32 MPa, (e) cohesion interval of 2.82–6.82 MPa, (f) cohesion interval of 3.32–6.32 MPa, (g) cohesion interval of 3.82–5.82 MPa, and (h) cohesion interval of 4.32–5.32 MPa.

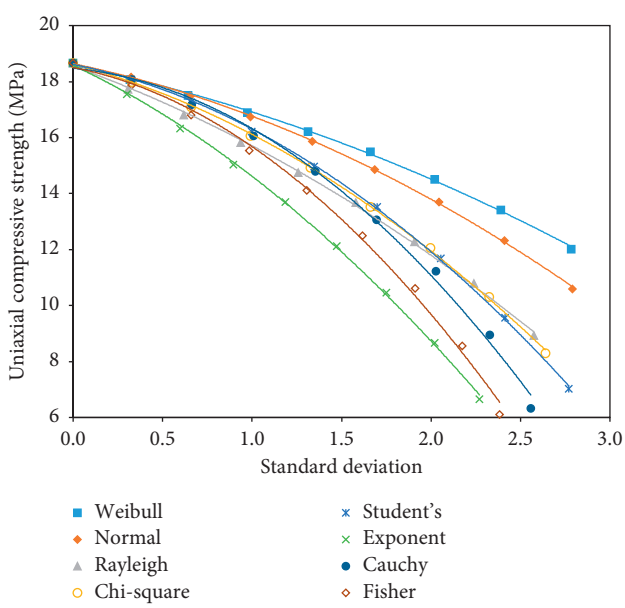

Figure 10: Variation of UCS of coal specimen versus the standard deviation.

purpose of Figure 10 is to provide a number of widely used probability distributions to study the heterogeneity based on their characteristics rather than list all of the existing distributions.

4.3. The Failure Characteristics of Coal Specimen with the Nonuniform Cohesion. In this study, shear strain rate (SSR) is employed to study the failure characteristics of coal specimens [57–59]. The SSR means square root of the second invariant of the deviatoric strain in FLAC^{3D} [60]. It is a FLAC^{3D} element variable in which the maximum SSR will return at each calculation step. The contours of SSR represent the most likely failure zone in which both the tensile and shear failure may occur. Figure 11 presents eight groups of stress-strain curves of coal specimen with nonuniform cohesion assignment by Weibull probability distribution. In these figures, the contours of SSR at different stages of the stress-strain curves are presented. The curve of the specimen with uniform cohesion is also presented as a comparison. It can be seen that the contours of SSR gradually distribute across the coal specimens when it reaches the postpeak strength. In addition, with the decrease of cohesion scatter degree, the change of one shear zone to two zones can be observed. It shows that the failure of coal specimen is more and more severe with the decrease of cohesion scatter degree. In other words, nonuniform cohesion reduces the coal strength and also reduces its failure intensity. Attention should be paid to the difference between homogeneous and heterogeneous specimens in terms of failure characteristics. It is suggested that the SSR is more regularly distributed in homogeneous specimens than that in heterogeneous specimens. The difference of these two kinds of specimens is that the heterogeneous specimen experiences more complex failure process than homogeneous specimen. It should be noted that the numerical simulation of failure characteristics of heterogeneous specimens is good agreement with the test results, as shown in Figure 12.

5. Discussion

5.1. A Suggested Coal Bursting Proneness Index. It can be revealed that the current indices used to identify bursting

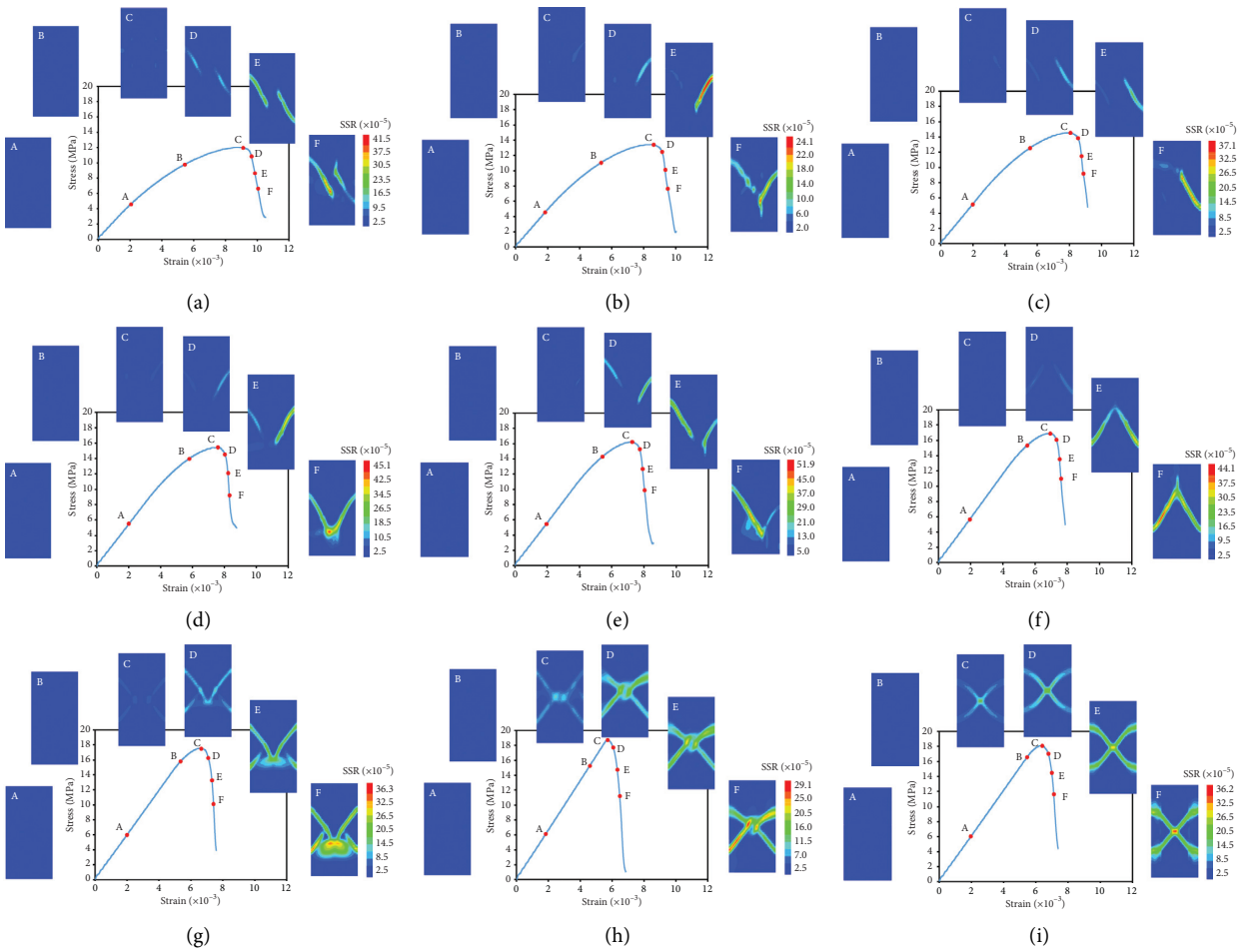

Figure 11: Eight groups of stress-strain curves of coal specimen with nonuniform cohesion assignment by Weibull probability distribution.

proneness have their own advantages and limitations. The index R_c can be directly used to determine bursting proneness. However, the released strain energy and the accumulated strain energy in the compressive test are not considered in this index. Although both K_E and W_{ET} are used to assess the bursting proneness with respect to the strain energy, W_{ET} focuses on the capacity of coal to absorb external inputs of energy before it achieves peak strength, while K_E considers not only the accumulated elastic energy before peak strength but also the energy released after the peak strength. The index D_t can reflect the speed of energy release, but it is not easy to be captured in the compressive test.

Su studied the influence of crystal size of material on the bursting proneness and concluded that the shear deformation associated with cohesion will influence the bursting proneness [61]. Zhang et al. simulated the yielding surface by changing the cohesion in the strain-softening model to study the coal burst risk in the coal pillar [62]. Hoek and Brown stated that the establishment of nonlinear failure criterion for intact rock should take account of the effect cohesion and friction [63]. Le et al. found that the whole process from initial yielding to final failure can be captured by considering the cohesive-frictional effect of the jointed rock [64]. Therefore, the cohesion and cohesive effect plays significant roles in the failure characteristics and process regardless of intact or jointed rocks.

According to the numerical and theoretical results in Figure 7, the functional equations can be established between all of the bursting proneness indices and cohesion. The high bursting proneness coal has relatively greater cohesion, and low bursting proneness coal has relatively lower cohesion. In addition, according to the linear functional relation between the indices of R_c and W_{ET} and the cohesion (see Figures 7(a) and 7(b)), it can be seen that the coal cohesion can be directly used to reflect the elastic strain energy accumulation before coal peak strength. Since the release of strain energy after peak strength is a nonlinear process, the indices of K_E and D_t have gradual and sharp variation stages with the variation of strain. The power functional equation between these two indices and cohesion can reflect this nonlinear characteristic (see Figures 7(c) and 7(d)).

Due to the inconsistency of identification results in the existing bursting proneness indexes, each identification index has certain limitations. Therefore, a new identification index is needed. According to the data given in Tables 2 and 4, the change of cohesion is most obvious in the change process of bursting proneness from high to none. Other

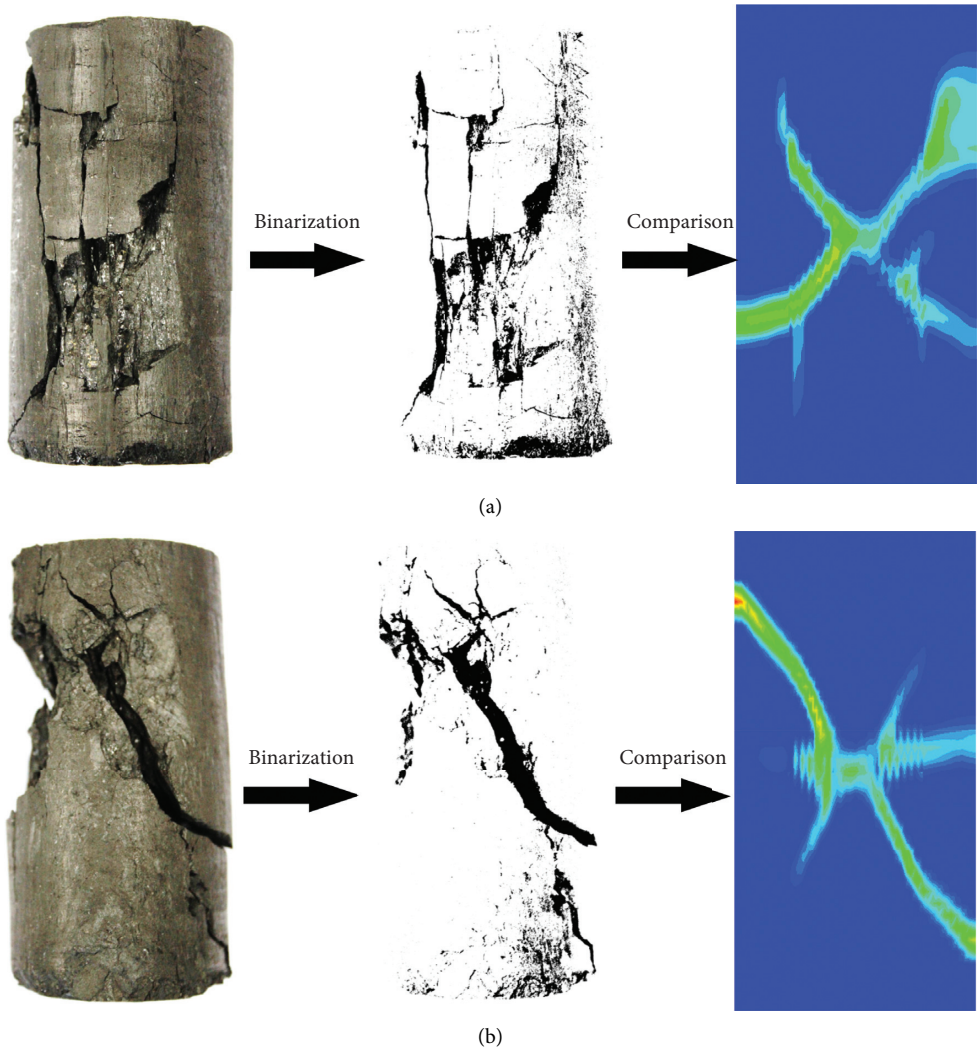

Figure 12: Comparison between the tests images and numerical results in terms of failure characteristics of coal specimens with bursting proneness: (a) high bursting proneness; (b) low bursting proneness.

scholars have also proved that there is an obvious corresponding relationship between bursting proneness and cohesion [61–63]. We also proved that there is a good correspondence between cohesive and bursting proneness through theoretical derivation. Therefore, cohesion can be used as an index to identify the bursting proneness, as listed in Table 8.

Figure 13 shows the contours of SSR after the peak strength calculated by FLAC^{3D} when the cohesion is uniformly distributed in coal specimens. The contours of SSR gradually transform from two zones to one zone when the cohesion changes from high to low. The shear strain zones distribute across the coal specimens when reaching the postpeak strength. In addition, the SSR of high bursting proneness coal is greater than that for the low or none bursting proneness coals. Since the bursting proneness can be identified by cohesion, the subfigures in Figure 13 are sequenced in order of cohesion. For example, as shown in Figure 13(a), specimens with cohesion of 6.07 MPa and 5.25 MPa are high bursting proneness coal and the specimens with 3.89 MPa, 3.03 MPa, and 2.79 MPa cohesion are low bursting proneness coal while 1.46 MPa specimen is the no bursting proneness coal.

The appearance of contours of SSR does not necessarily mean that the shear failure will occur along the zones. The contours of plastic state after the peak strength are calculated to further study the failure characteristics. As shown in Figure 13(b), in the legend, shear-n and tension-n are abbreviations of shear-now and tension-now, indicating the position where shear plastic strain and tensile plastic strain are occurring; shear-p and tension-p are abbreviations of shear-past and tension-past, indicating the position where shear plastic strain and tensile plastic strain have occurred. The results show that there are more tensile failure zones in the coal specimens with high or low bursting proneness and there are more shear failure zones in the coal specimens with no bursting proneness. Therefore, the failure of high bursting proneness coal is more violent than that for the low or no bursting proneness coal. The failure characteristics are gradual variation from

Table 8: Cohesion used to identify the bursting proneness of coal.

Indices	No bursting proneness	Low bursting proneness	High bursting proneness
Cohesion (C) (MPa)	$C < 1.5$	$1.5 \leq C < 4.0$	$C \geq 4.0$

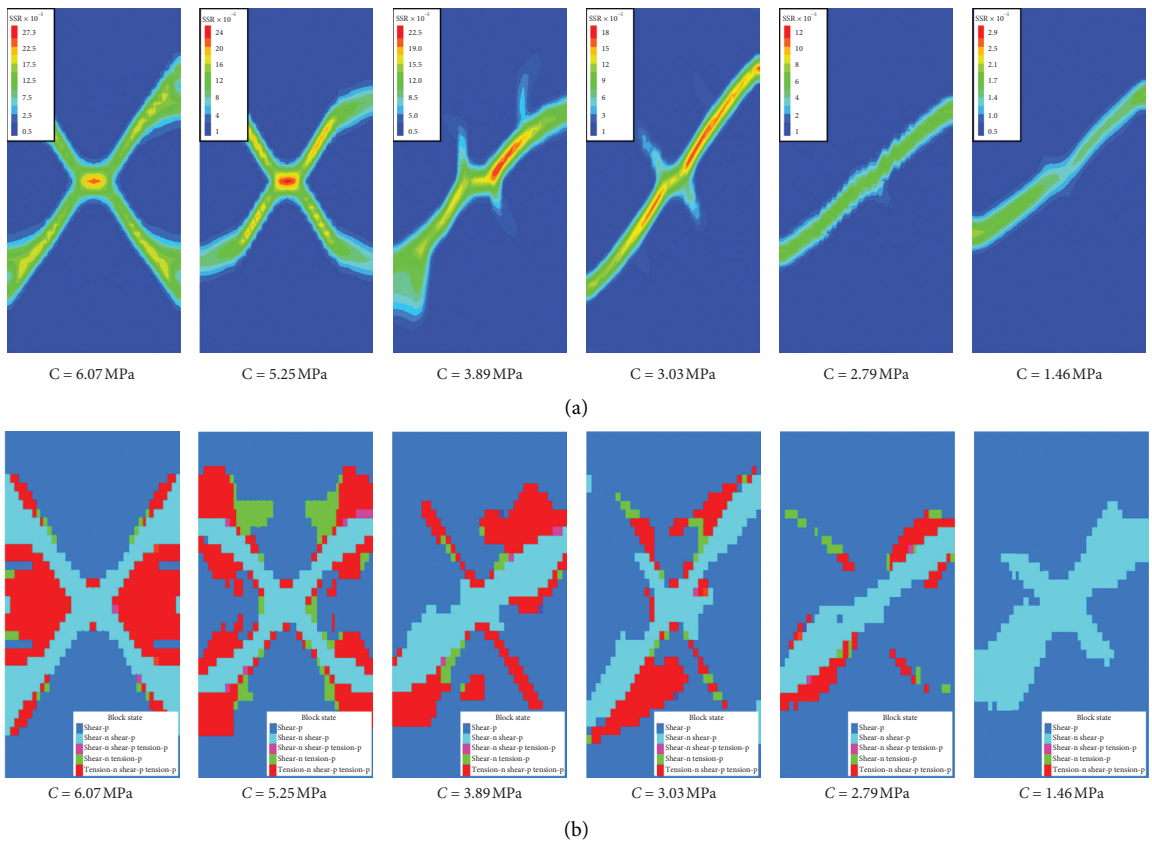

Figure 13: Contours of SSR and plastic zones calculated by FLAC^{3D} for coal specimens with different cohesion: (a) contours of SSR; (b) plastic zones.

tensile failure to shear failure when the bursting proneness changes from high to none.

5.2. Assignment Method of Nonuniform Coal Cohesion to the Numerical Model. As shown in Figure 8, nonuniform cohesion is assigned to the numerical model from t center to edge of cross section according to the distribution functions. However, since the cohesion is quite randomly distributed in coal, it is necessary to study the influence of the random distribution of cohesion on the coal UCS or bursting proneness. Taking the No. 12 coal specimen as an example, the cohesion will be randomly distributed in the numerical model by Weibull function. The parameter m is set from 2 to 10, and the x_0 is set as 4.82 MPa for the cohesion of this specimen. Figure 14 presents cohesion assignment in the numerical model with the different parameter m. It can be seen that the distribution of cohesion tends to be more uniform in the numerical model with the increasing of parameter m. Therefore, the implication of Figure 14 is that the scatter degree of coal properties can be adjusted by the parameters m when using the Weibull function. The smaller the parameter m is, the greater the scatter degree of coal properties will be.

Figure 15 shows the stress-strain curves of No. 12 coal specimen under the random assignment of cohesion by Weibull function. The curve of the specimen with uniform cohesion is also presented as a comparison. In this figure, the modeling results suggest that, since the scatter degree of cohesion in the numerical model will increase with the increasing of m value, the UCS of coal specimen increases with the increasing of parameter m. However, there is not much difference in the UCS of coal specimen for each parameter m under the method of random assignment of cohesion to the numerical model. Figure 16 shows the plastic strain contour of the specimen under different m parameters. It can be seen from the figure that when m is small, the plastic strain will occur at all positions of the specimen due to the large scatter degree of cohesion. When m is large, the failure mode of the specimen is similar to the homogeneous model due to the small dispersion of cohesion, and the plastic strain is concentrated in one or two strips. Therefore,

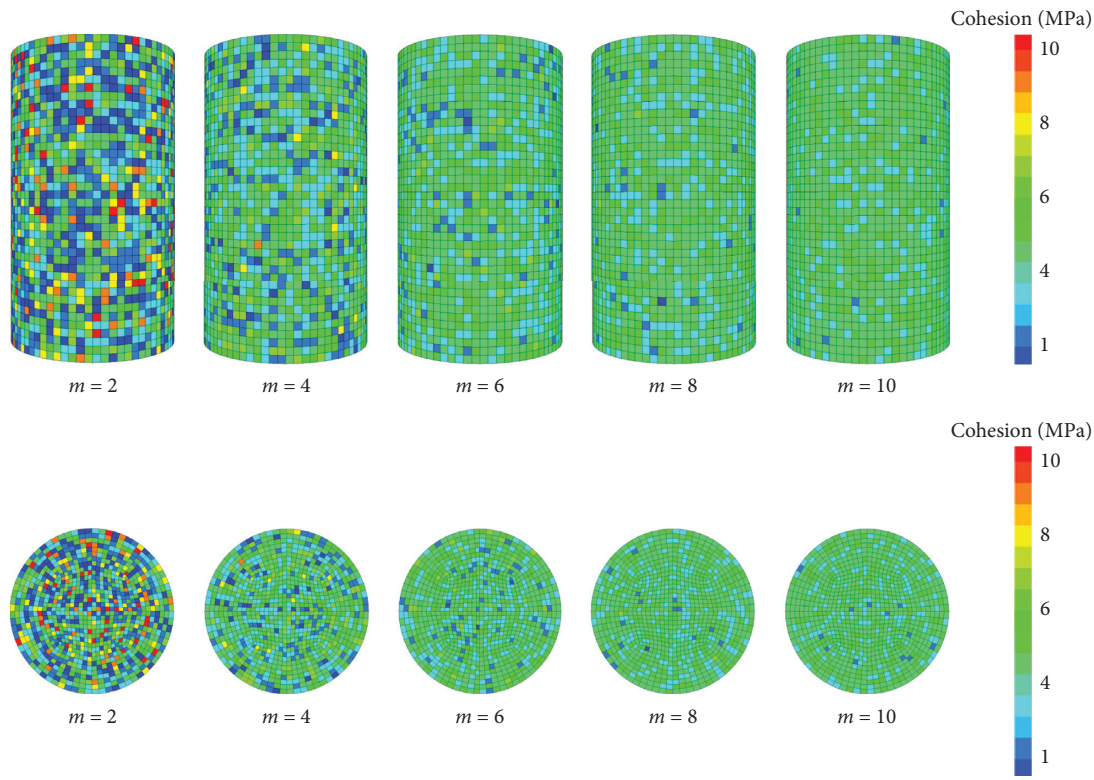

Figure 14: Random assignment of cohesion in the numerical model by Weibull function with different parameter m.

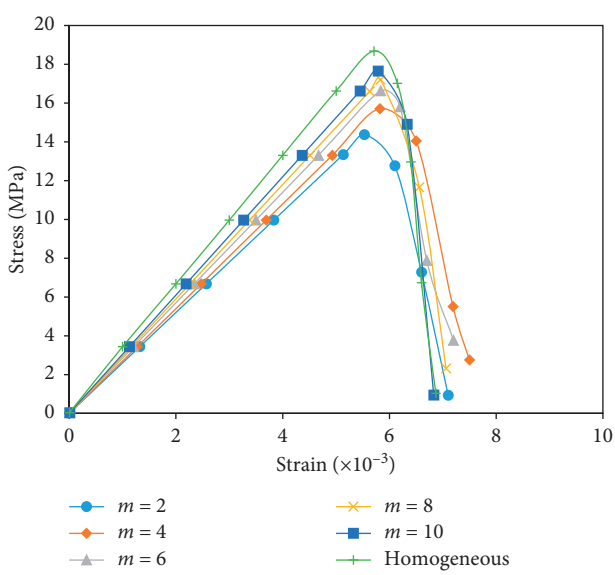

Figure 15: Stress-strain curves of No. 12 coal specimen under random assignment of cohesion by Weibull function.

it can be considered that when m is small, the ultimate failure mode of the specimen is fragmentation failure, while when m is large, the ultimate failure mode of the specimen is splitting failure caused by one or two main cracks.

By comparing the stress-strain curves of Figures 9 and 15, it can be seen that the large variation of UCS can be observed by the assignment method from the model center to edge. The assignment method from the model center to edge is to place a group of smaller cohesion at the edge of the numerical model and a group of larger cohesion at the center of the model. The method of random assignment does not determine the position of cohesion in the numerical model in advance. Therefore, the numerical model may be failed gradually from edge to center under the assignment method from the model center to edge. The failure of numerical model does not necessarily follow this pattern under the method of random assignment of cohesion, as shown in Figure 17.

Figure 17(a) shows the SSR contour from the center to the edge with the interval of 1.32 MPa–8.32 MPa, and Figure 17(b) shows the random assignment SSR contour with $m = 2$. It can be seen from Figure 17(a) that, by employing the method of assignment from center to edge, the edges of the model begin to fail under the axial compressive pressure and the failure zones gradually develop from edge to center until the model is completely destroyed. However, Figure 17(b) shows that the failure zones appear first at the center of the numerical model which is assigned the parameters randomly. It is important to point out that, since the numerical parameters are randomly assigned to model, the failure zones may be different from the Figure 17(b) if the next assignment is conducted. In addition, it should be noted that the purpose of this comparison is to provide two methods of numerical parameters assignment to model rather than evaluating the advantages or disadvantages of these two methods.

5.3. Analyses of Factors Contributing to Coal Bursts. As discussed previously in this paper, coal bursts are closely related to the intrinsic bursting proneness of coal

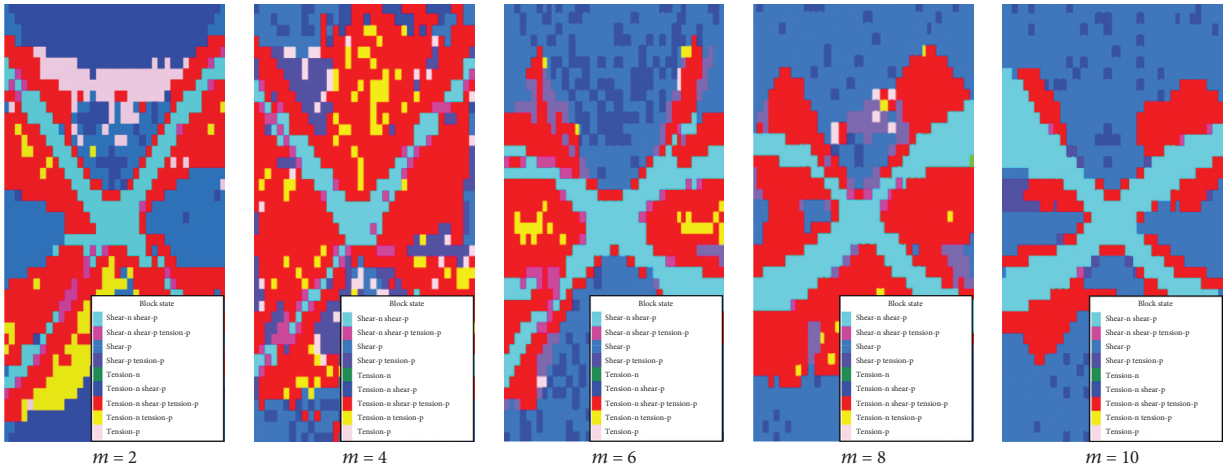

Figure 16: Plastic strain contour of No. 12 coal specimen under random assignment of cohesion by Weibull function.

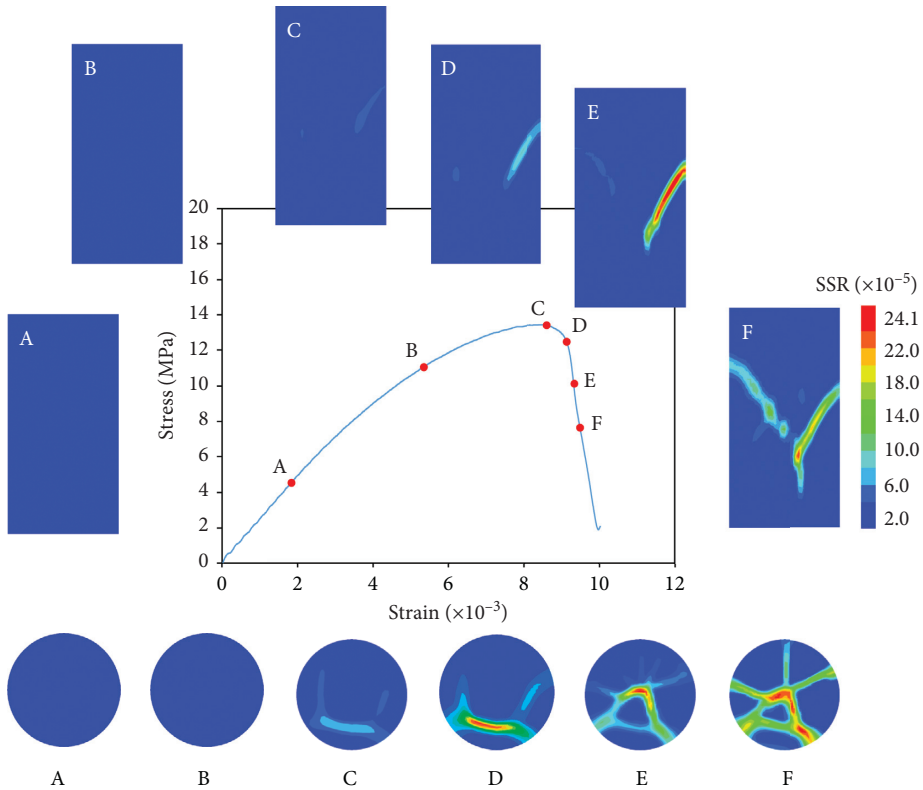

(a)

Figure 17: Continued.

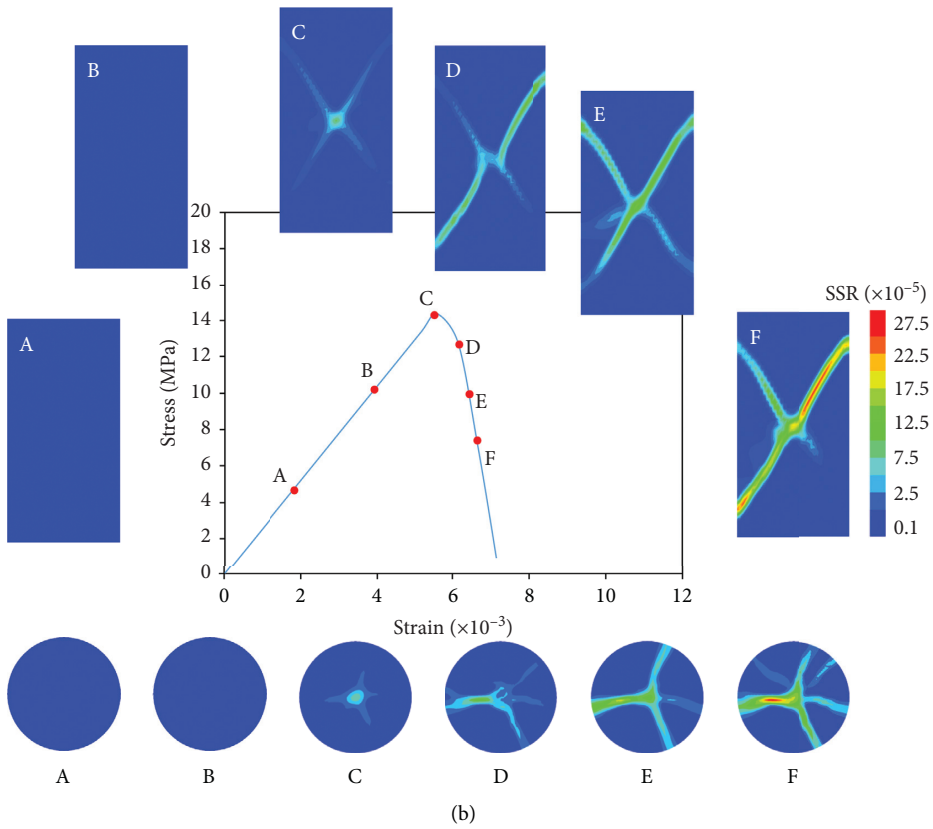

Figure 17: Comparison of model failure pattern between the method of parameter assignment from center to edge and random assignment: (a) assignment from center to edge; (b) random assignment.

[4, 5, 7, 12–18]. In addition, the failure characteristics of coal specimens show that the high bursting proneness coal includes tension, shear, and mixed tension-shear failures. However, Mark and Gauna pointed out that the occurrence of coal bursts is combined results of highly stressed environments [1]. Wang et al. found that no coal burst has been observed in some coal seams identified as high bursting proneness [15]. Afraei et al. stated that overburden thickness, stress state, and rock properties are the available factors to influence the prediction of coal bursts [34]. As shown in Table 2, the statistics of geological conditions of coal specimens suggests that large amounts of faults, primary folds, subsidiary fold structures, overturned rock strata, extreme thick roof strata, and island longwall mining face can be detected in most of the coal mines. These geological conditions are significant external factors contributing to the occurrence of coal bursts. On November 3, 2011, a severe coal burst accident occurred in the Qianqiu coal mine of Yima mining area, Henan Province, China, and it is believed that the frequent large reverse fault reactivation and slip contribute to these coal bursts [6, 32, 65–69].

In conclusion, a coal burst is the interactional results of bursting proneness, unstable geological structure, extreme thick roof strata, and island longwall mining face. In addition, due to the greater cohesion between the particles in coal specimens, coal with high bursting proneness provides an ideal internal environment for energy accumulation. To weaken this environment, the technologies including coal seam softening by water injection, borehole drilling in front of mining face, and advanced blasting in coal seam are wildly applied in coal mines to eliminate the bursting proneness [70–73].

6. Conclusions

Relationship between the coal bursting proneness and coal homogeneity and heterogeneity are studied in this paper. The main conclusions are summarized as follows:

(1) By numerically fitting the stress-strain curves of 27 coal specimens, the relationship between bursting proneness indices and cohesion of coal is statically established and the functional equations between them are theoretically obtained. It is suggested that the proneness indices R_c and W_{ET} linearly increase with the increase of cohesion while the index K_E and cohesion have a positive power function relation. However, the negative power function between the index D_t and cohesion is established.

(2) The linear functional relation between the indices of R_c and W_{ET} and the cohesion suggests that the cohesion of coal can be directly used to reflect the elastic strain energy accumulation before coal peak strength. In addition, because of the power functional equation between cohesion and K_E and D_t, the

coal cohesion could also be used to illustrate the nonlinear process of strain energy release after peak strength. Therefore, coal cohesion combines the common advantages of the four indices and it can be used as an index to identify the bursting proneness. It is suggested that coal is of high bursting proneness when the cohesion is greater than 4.0 MPa and the low bursting proneness is warranted when the cohesion is greater than 1.5 MPa.

(3) By taking into account the coal heterogeneity, eight probability distribution functions are employed to assign the cohesion to the numerical model and to study the influence of heterogeneity on the bursting proneness. With the increasing of cohesion scatter degree, the UCS decrement of heterogeneous coal specimen assigned by Weibull and Normal distributions was smaller than that by the other six distributions. The UCS of heterogeneous coal specimen with Fisher distribution decreases fastest among the other distributions with the increasing of cohesion scatter degree. The coal bursting proneness will decrease with the increasing of cohesion scatter degree. The larger the cohesion scatter degree increase is, the lower the bursting proneness will be. The failure of coal specimen is more and more severe with the decrease of cohesion scatter degree.

(4) There are many methods to assign heterogeneous parameters to the numerical models. This study provides two methods including the assignment from center to edge and random assignment. The selection of different method determines the different failure characteristics of the numerical model. By employing the method of assignment from center to edge, the edges of the model begin to fail and the failure zones gradually develop from edge to center until the model is completely destroyed. The selection of random assignment may simulate the characteristics in which failure zones appear first at the center of the numerical model.

(5) The underground coal seam with high bursting proneness provides an ideal internal environment for energy accumulation. The high bursting proneness may be just an internal factor inducing coal burst accidents while the geological conditions are the significant external factors contributing to the occurrence of coal bursts. Therefore, the coal bursts are the interactional results of high bursting proneness, unstable geological structure including thrust faults and overturned folds, extreme thick roof strata, and island longwall panel mining.

Data Availability

The data used to support the findings of this study are included within the article.

Conflicts of Interest

The authors declare that they have no conflicts of interest.

Acknowledgments

This research was financially supported by the National Natural Science Foundation of China (41872205), Beijing Natural Science Foundation (8202041), Yue Qi Young Scholar Project, China University of Mining & Technology, Beijing (2018QN13), and the Fundamental Research Funds for the Central Universities (2021YJSLJ10).

References

[1] C. Mark and M. Gauna, "Evaluating the risk of coal bursts in underground coal mines," *International Journal of Mining Science and Technology*, vol. 26, no. 1, pp. 47–52, 2016.

[2] C. Mark, "Coal bursts in the deep longwall mines of the United States," *International Journal of Coal Science & Technology*, vol. 3, no. 1, pp. 1–9, 2016.

[3] H. W. Wang, Y. D. Jiang, S. Xue et al., "Investigation of intrinsic and external factors contributing to the occurrence of coal bumps in the mining area of western Beijing, China," *Rock Mechanics and Rock Engineering*, vol. 50, no. 4, pp. 1033–1047, 2017.

[4] O. Vardar, C. Zhang, I. Canbulat, and B. Hebblewhite, "A semi-quantitative coal burst risk classification system," *International Journal of Mining Science and Technology*, vol. 28, no. 5, pp. 721–727, 2018.

[5] A. Mottahedi and M. Ataei, "Fuzzy fault tree analysis for coal burst occurrence probability in underground coal mining," *Tunnelling and Underground Space Technology*, vol. 83, pp. 165–174, 2019.

[6] R. Frith, G. Reed, and A. Jones, "A causation mechanism for coal bursts during roadway development based on the major horizontal stress in coal: very specific structural geology causing a localised loss of effective coal confinement and Newton's second law," *International Journal of Mining Science and Technology*, vol. 30, no. 1, pp. 39–47, 2020.

[7] C. Mark, "Coal bursts that occur during development: a rock mechanics enigma," *International Journal of Mining Science and Technology*, vol. 28, no. 1, pp. 35–42, 2018.

[8] S. He, D. Song, and Z. Li, "Precursor of spatio-temporal evolution law of MS and AE activities for rock burst warning in steeply inclined and extremely thick coal seams under caving mining conditions," *Rock Mechanics and Rock Engineering*, vol. 52, no. 7, pp. 2415–2435, 2019.

[9] G. Y. Ren, "Analysis of "10.20" major accident in Shandong Longyun coal industry co., ltd. of Shandong energy group," *Jilin Labour Protection*, vol. 4, pp. 41–46, 2019.

[10] J. G. Lv, Y. D. Jiang, and S. G. Li, "Characteristics and mechanism research of coal bumps induced by faults based on extra thick and hard roof," *Journal of China Coal Society*, vol. 39, no. 10, pp. 1961–1969, 2014.

[11] H. Bruce and G. Jim, "A review of the geomechanics aspects of a double fatality coal burst at Austar Colliery in NSW, Australia in April 2014," *International Journal of Mining Science and Technology*, vol. 27, no. 1, pp. 3–7, 2017.

[12] Y. Jiang, Y. Zhao, H. Wang, and J. Zhu, "A review of mechanism and prevention technologies of coal bumps in China," *Journal of Rock Mechanics and Geotechnical Engineering*, vol. 9, no. 1, pp. 180–194, 2017.

[13] A. W. Khair, "An analysis of coal bump liability in a bump prone mine," *International Journal of Mining Engineering*, vol. 3, no. 4, pp. 243–259, 1958.

[14] M. He, H. Xia, X. Jia, W. Gong, F. Zhao, and K. Liang, "Studies on classification, criteria and control of rockbursts," *Journal of*

Rock Mechanics and Geotechnical Engineering, vol. 4, no. 2, pp. 97–114, 2012.

[15] H. Wang, Y. Jiang, and S. Xue, "Influence of fault slip on mining-induced pressure and optimization of roadway support design in fault-influenced zone," *Journal of Rock Mechanics and Geotechnical Engineering*, vol. 8, no. 5, pp. 660–671, 2016.

[16] X. Yang, T. Ren, L. Tan, A. Remennikov, and X. He, "Developing coal burst propensity index method for Australian coal mines," *International Journal of Mining Science and Technology*, vol. 28, no. 5, pp. 783–790, 2018.

[17] GB/T 25217.2-2010, *Classification and Laboratory Test Method on Bursting Liability of Coal*, Standards Press of China, Beijing, China, 2010.

[18] A. Kidybiński, "Bursting liability indices of coal," *International Journal of Rock Mechanics and Mining Sciences & Geomechanics Abstracts*, vol. 18, no. 4, pp. 295–304, 1981.

[19] H. Lippmann, "Mechanics of "bumps" in coal mines: a discussion of violent deformations in the sides of roadways in coal seams," *Applied Mechanics Reviews*, vol. 40, no. 8, pp. 1033–1043, 1987.

[20] K. Y. Haramy and J. P. McDonnell, *Causes and Control of Coal Mine Bumps*, Bureau of Mines, Denver, CO, USA, 1988.

[21] S. P. Singh, "Burst energy release index," *Rock Mechanics and Rock Engineering*, vol. 21, no. 2, pp. 149–155, 1998.

[22] S. M. Lee, B. S. Park, and S. W. Lee, "Analysis of rockbursts that have occurred in a waterway tunnel in Korea," *International Journal of Rock Mechanics and Mining Sciences*, vol. 41, pp. 911–916, 2004.

[23] C. D. Su, R. F. Yuan, and X. X. Zhai, "Experimental research on bursting liability index of coal samples of Chengjiao coal mine," *Chinese Journal of Rock Mechanics and Engineering*, vol. 41, no. S2, pp. 3696–3704, 2013.

[24] L. Z. Tang, C. L. Pan, and W. X. Wang, "Surplus energy index for analysing rock burst proneness," *Journal of Central South University of Technology*, vol. 3, no. 2, pp. 129–132, 2002.

[25] X. Y. Zhang, G. R. Feng, L. X. Kang, and S. S. Yang, "Method to determine burst tendency of coal rock by residual energy emission speed," *Journal of China Coal Society*, vol. 34, no. 9, pp. 1165–1168, 2009.

[26] F. Q. Gong, J. Y. Yan, and X. B. Li, "A new criterion of rock burst proneness based on the linear energy storage law and the residual elastic energy index," *Chinese Journal of Rock Mechanics and Engineering*, vol. 37, no. 9, pp. 1993–2014, 2018.

[27] M. Aubertin, D. E. Gill, and R. Simon, "On the use of the brittleness index modified (BIM) to estimate the post-peak behavior of rocks," in *Proceedings of the 1st North American Rock Mechanics Symposium*, Austin; TX, USA, 1994.

[28] L. Z. Tang and W. X. Wang, "New rock burst proneness index," *Chinese Journal of Rock Mechanics and Engineering*, vol. 21, no. 6, pp. 874–878, 2002.

[29] Y. S. Pan, L. Geng, and Z. H. Li, "Research on evaluation indices for impact tendency and danger of coal seam," *Jorunal of China Coal Society*, vol. 35, no. 12, pp. 1975–1978, 2010.

[30] F. Gao, Z. Z. Zhang, and X. G. Liu, "Research on rock burst proneness index based on energy evolution in rock," *Disaster Advances*, vol. 5, no. 4, pp. 1367–1371, 2012.

[31] Q. X. Qi, Y. H. Peng, H. Y. Li et al., "Study of bursting liability of coal and rock," *Chinese Journal of Rock Mechanics and Engineering*, vol. 30, no. S1, pp. 2736–2742, 2011.

[32] W. Cai, L. Dou, A. Cao, S. Gong, and Z. Li, "Application of seismic velocity tomography in underground coal mines: a case study of Yima mining area, Henan, China," *Journal of Applied Geophysics*, vol. 109, pp. 140–149, 2014.

[33] R. S. Faradonbeh and A. Taheri, "Long-term prediction of rockburst hazard in deep underground openings using three robust data mining techniques," *Engineering with Computers*, vol. 2, pp. 1–17, 2018.

[34] S. Afraei, K. Shahriar, and S. H. Madani, "Statistical assessment of rock burst potential and contributions of considered predictor variables in the task," *Tunnelling and Underground Space Technology*, vol. 72, pp. 250–271, 2018.

[35] W. J. Gale, "A review of energy associated with coal bursts," *International Journal of Mining Science and Technology*, vol. 28, no. 5, pp. 755–761, 2018.

[36] Z.-z. Zhang, F. Gao, and X.-j. Shang, "Rock burst proneness prediction by acoustic emission test during rock deformation," *Journal of Central South University*, vol. 21, no. 1, pp. 373–380, 2014.

[37] J. Li, J. Yue, Y. Yang, X. Zhan, and L. Zhao, "Multi-resolution feature fusion model for coal rock burst hazard recognition based on acoustic emission data," *Measurement*, vol. 100, pp. 329–336, 2017.

[38] X. Liu, X. Wang, and E. Wang, "Effects of gas pressure on bursting liability of coal under uniaxial conditions," *Journal of Natural Gas Science and Engineering*, vol. 39, pp. 90–100, 2017.

[39] Z. Z. Feng and Y. S. Zhao, "Correlativity of rock inhomogeneity and rock burst trend," *Chinese Journal of Rock Mechanics and Engineering*, vol. 22, no. 11, pp. 1863–1865, 2003.

[40] J. L. Pan, F. H. Ren, and M. F. Cai, "Effect of joint density on rockburst proneness of the elastic-brittle-plastic rock mass," *Shock and Vibration*, vol. 2021, Article ID 5574325, 9 pages, 2021.

[41] J. Pan, Z. Meng, Q. Hou, Y. Ju, and Y. Cao, "Coal strength and Young's modulus related to coal rank, compressional velocity and maceral composition," *Journal of Structural Geology*, vol. 54, pp. 129–135, 2013.

[42] C. D. Su, X. X. Chen, and R. F. Yuan, "Analysis of deformation and strength characteristics of coal samples under uniaxial compression of stepped relaxation," *Chinese Journal of Rock Mechanics and Engineering*, vol. 33, no. 6, pp. 1135–1141, 2014.

[43] X. Song, X. Li, and Z. Li, "Study on the characteristics of coal rock electromagnetic radiation (EMR) and the main influencing factors," *Journal of Applied Geophysics*, vol. 148, pp. 216–225, 2018.

[44] J. N. Pan, Z. P. Meng, and B. M. Liu, "Relationship between rock composition and texture of coal-bearing formation and its burst potential," *Chinese Journal of Rock Mechancis and Engineering*, vol. 24, pp. 4422–4427, 2005.

[45] J. Zhang, C. Ai, Y.-w. Li, M.-g. Che, R. Gao, and J. Zeng, "Energy-based brittleness index and acoustic emission characteristics of anisotropic coal under triaxial stress condition," *Rock Mechanics and Rock Engineering*, vol. 51, no. 11, pp. 3343–3360, 2018.

[46] H. Li, H. Li, B. Gao, D. Jiang, and J. Feng, "Study of acoustic emission and mechanical characteristics of coal samples under different loading rates," *Shock and Vibration*, vol. 2015, Article ID 458519, 11 pages, 2015.

[47] S. Okubo, K. Fukui, and Q. Qingxin, "Uniaxial compression and tension tests of anthracite and loading rate dependence of peak strength," *International Journal of Coal Geology*, vol. 68, no. 3-4, pp. 196–204, 2006.

[48] C. D. Su, B. B. Gao, R. F. Yuan et al., "Outburst-proneness index and their correlation analysis of coal seams in Pingdingshan mine area," *Journal of China Coal Society*, vol. 39, no. S1, pp. 8–14, 2014.

[49] C. D. Su, B. H. Guo, and X. Tang, "Research on acoustic emission characteristics of Zhangcun coal samples in two sizes subject to uniaxial compression," *Journl of China Coal Society*, vol. 38, no. S1, pp. 12–18, 2013.

[50] H. B. Xie, Y. F. Xu, and J. W. Kang, "Relationship between vitrinite reflectance of deformed coal and palaeotectonic stress field in western Henan coalfield," *Coal Geology and Exploration*, vol. 36, no. 4, pp. 1–4, 2006.

[51] S. P. Li, *A Brief Introduction to Rock Mechanics*, China University of Mining and Technology Press, Xuzhou, China, 1986.

[52] S. M. Wang, H. H. Zhu, X. T. Feng et al., "Influence of heterogeneity on macroscopical crack form of the brittle rock," *Rock & Soil Mechanics*, vol. 27, no. 2, pp. 224–227, 2006.

[53] R. Luo, Y. W. Zeng, and X. Du, "Relationship between macroscopic and mesoscopic mechanical parameters of inhomogenous rock material," *Chinese Journal of Geotechnical Engineering*, vol. 34, no. 12, pp. 2331–2336, 2012.

[54] M. Y. Li, W. Q. Shen, and J. F. Shao, "A numerical study of effective mechanical behaviors of rock like materials based on fast Fourier transform," *Mechanics of Materials*, vol. 92, no. 5, pp. 275–288, 2016.

[55] P. Q. Ji, X. P. Zhang, and Q. Zhang, "A new method to model the non-linear crack closure behavior of rocks under uniaxial compression," *International Journal of Rock Mechanics and Mining Sciences*, vol. 112, pp. 171–183, 2018.

[56] S.-Q. Yang, P.-F. Yin, Y.-C. Zhang et al., "Failure behavior and crack evolution mechanism of a non-persistent jointed rock mass containing a circular hole," *International Journal of Rock Mechanics and Mining Sciences*, vol. 114, pp. 101–121, 2019.

[57] Y. Zhao, S. Liu, G.-F. Zhao, D. Elsworth, Y. Jiang, and J. Han, "Failure mechanisms in coal: dependence on strain rate and microstructure," *Journal of Geophysical Research: Solid Earth*, vol. 119, no. 9, pp. 6924–6935, 2014.

[58] H. Wagner, "Deep mining: a rock engineering challenge," *Rock Mechanics and Rock Engineering*, vol. 52, no. 5, pp. 1417–1446, 2019.

[59] B. Shen, J. Shi, and N. Barton, "An approximate nonlinear modified Mohr-Coulomb shear strength criterion with critical state for intact rocks," *Journal of Rock Mechanics and Geotechnical Engineering*, vol. 10, no. 4, pp. 645–652, 2018.

[60] Itasca Consulting Group Inc, *FLAC3D, (Fast Lagrangian Analysis of Continua in 3 Dimensions)*, Itasca Consulting Group Inc, Minneapolis, MN, USA, 2006.

[61] C. D. Su, "Testing study on the effect of crystal size and specimen length on the rockburst tendency," *Chinese Journal of Rock Mechanics and Engineering*, vol. 23, no. 22, pp. 3750–3753, 2004.

[62] C. Zhang, I. Canbulat, F. Tahmasebinia, and B. Hebblewhite, "Assessment of energy release mechanisms contributing to coal burst," *International Journal of Mining Science and Technology*, vol. 27, no. 1, pp. 43–47, 2017.

[63] E. Hoek and E. T. Brown, "The Hoek-Brown failure criterion and GSI—2018 edition," *Journal of Rock Mechanics and Geotechnical Engineering*, vol. 11, no. 3, pp. 445–463, 2019.

[64] L. A. Le, G. D. Nguyen, H. H. Bui, A. H. Sheikh, A. Kotousov, and A. Khanna, "Modelling jointed rock mass as a continuum with an embedded cohesive-frictional model," *Engineering Geology*, vol. 228, pp. 107–120, 2017.

[65] H. W. Wang, S. Xue, R. M. Shi, Y. Jiang, W. Gong, and L. Mao, "Investigation of fault displacement evolution during extraction in longwall panel in an underground coal mine," *Rock Mechanics and Rock Engineering*, vol. 53, pp. 1809–1826, 2019.

[66] B. T. Shen, Y. Duan, X. Luo et al., "Monitoring and modelling stress state near major geological structures in an underground coal mine for coal burst assessment," *International Journal of Rock Mechanics and Mining Sciences*, vol. 129, Article ID 104294, 2020.

[67] L. M. Dou, Y. He, and W. Zhang, "Hazards of rock burst in island coal face and its control," *Chinese Journal of Rock Mechanics and Engineering*, vol. 11, pp. 1866–1869, 2003.

[68] H. W. Wang, R. M. Shi, D. X. Deng, Y. Jiang, G. Wang, and W. Gong, "Characteristic of stress evolution on fault surface and coal bursts mechanism during the extraction of longwall face in Yima mining area, China," *Journal of Structural Geology*, vol. 136, Article ID 104071, 2020.

[69] J. G. Lv, C. Q. Nan, Y. Zhang et al., "Coal bump mechanism in Yima coalfield mining near thrust fault," *Journal of Mining and Safety Engineering*, vol. 35, no. 3, pp. 567–574, 2018.

[70] Y. He, F. Peng, X. J. Hu et al., "Monitoring and control of rock burst in island coving coal face," *Journal of China University of Mining and Technology*, vol. 5, pp. 593–596, 2004.

[71] W.-m. Cheng, W. Nie, G. Zhou, Y. Yu, Y. Ma, and J. Xue, "Research and practice on fluctuation water injection technology at low permeability coal seam," *Safety Science*, vol. 50, no. 4, pp. 851–856, 2012.

[72] Ł. Wojtecki, P. Konicek, and J. Schreiber, "Effects of torpedo blasting on rockburst prevention during deep coal seam mining in the upper Silesian coal basin," *Journal of Rock Mechanics and Geotechnical Engineering*, vol. 9, no. 4, pp. 694–701, 2017.

[73] D. Song, E. Wang, X. He et al., "Use of electromagnetic radiation from fractures for mining-induced stress field assessment," *Journal of Geophysics and Engineering*, vol. 15, no. 4, pp. 1093–1103, 2018.